University of Tennessee, Knoxville
TRACE: Tennessee Research and Creative Exchange

Doctoral Dissertations | Graduate School

12-2008

Label-free mapping of near-field transport properties of micro/nano-fluidic phenomena using surface plasmon resonance (SPR) reflectance imaging

Iltai Kim
University of Tennessee - Knoxville

Follow this and additional works at: https://trace.tennessee.edu/utk_graddiss

 Part of the Mechanical Engineering Commons

Recommended Citation

Kim, Iltai, "Label-free mapping of near-field transport properties of micro/nano-fluidic phenomena using surface plasmon resonance (SPR) reflectance imaging. " PhD diss., University of Tennessee, 2008.
https://trace.tennessee.edu/utk_graddiss/557

This Dissertation is brought to you for free and open access by the Graduate School at TRACE: Tennessee Research and Creative Exchange. It has been accepted for inclusion in Doctoral Dissertations by an authorized administrator of TRACE: Tennessee Research and Creative Exchange. For more information, please contact trace@utk.edu.

To the Graduate Council:

I am submitting herewith a dissertation written by Iltai Kim entitled "Label-free mapping of near-field transport properties of micro/nano-fluidic phenomena using surface plasmon resonance (SPR) reflectance imaging." I have examined the final electronic copy of this dissertation for form and content and recommend that it be accepted in partial fulfillment of the requirements for the degree of Doctor of Philosophy, with a major in Mechanical Engineering.

Kenneth D. Kihm, Major Professor

We have read this dissertation and recommend its acceptance:

Majid Keyhani, Jayne Wu, Thomas L. Ferrell

Accepted for the Council:

Carolyn R. Hodges

Vice Provost and Dean of the Graduate School

(Original signatures are on file with official student records.)

To the Graduate Council:

I am submitting herewith a dissertation written by Iltai Kim entitled “Label-free mapping of near-field transport properties of micro/nano-fluidic phenomena using surface plasmon resonance (*SPR*) reflectance imaging.” I have examined the final electronic copy of this dissertation for form and content and recommended that it be accepted in partial fulfillment of the requirements for the degree of Doctor of Philosophy, with a major in Mechanical Engineering.

Kenneth D. Kihm
Major Professor

We have read this dissertation
and recommend its acceptance:

Majid Keyhani

Jayne Wu

Thomas L. Ferrell

Accepted for the council:

Carolyn R. Hodges
Vice Provost and Dean of
Graduate Studies

(Original signatures are on file with official student records.)

Label-free mapping of near-field transport properties of micro/nano-fluidic phenomena using surface plasmon resonance (*SPR*) reflectance imaging

A Dissertation
Presented for the
Doctor of Philosophy
Degree
The University of Tennessee, Knoxville

Iltai Kim
December 2008

DEDICATION

To my wife Hyun Soo Kwon,
my daughter Shiyeon, my sons Yongsam & Gwangsan, my parents,
and my precious Lord Jesus Christ.

ACKNOWLEDGEMENTS

I would like to give my sincere appreciation and gratitude to my advisor Dr. Kenneth D. Kihm for his continuous support, encouragement, valuable advices, and stimulating discussions throughout the course of this study. Also, I give sincere appreciation and thanks to my dissertation committee members, Dr. Majid Keyhani, Dr. Jayne Wu, and Dr. Thomas L. Ferrell for their advice and constructive comments and voluntary services.

Special thanks are expressed to the MINSFET Lab former and current members who worked and spent time with, Dr. Sangkwon Wee, Dr. Sokwon Paik, Dr. Jaesung Park, Dr. Chanhee Chon, Dr. Changkyoung Choi, Dr. Seonghwan Kim, Dr. Chuck Margraves, Dr. S. Y. Yoon, Mr. Joseph Tipton, Jr. and Mr. Hunju Yi.

I wish to extend my thanks to my parents and parents-in-law for their continuing support and prayer. Lastly, I would like to express my love and appreciation to my wonderful wife, Hyun Soo Kwon for her sacrifice, patience, trust, and love.

ABSTRACT

My doctoral research has focused on the development of surface plasmon resonance (*SPR*) reflectance imaging technique to detect near-field transport properties such as concentration, temperature, and salinity in micro/nano fluidic phenomena in label-free, real-time, and full-field manner.

A label-free visualization technique based on surface plasmon resonance (*SPR*) reflectance sensing is presented for real-time and full-field mapping of microscale concentration and temperature fields. The key idea is that the *SPR* reflectance sensitivity varies with the refractive index of the near-wall region of the test mixture fluid. The Fresnel equation, based on Kretschmann's theory, correlates the *SPR* reflectance with the refractive index of the test medium, and then, the refractive index correlates with the mixture concentration or temperature. The basic operation principle is summarized and the laboratory-developed *SPR* imaging/analyzing system is described with the measurement sensitivity, uncertainties and detection limitations of the implemented *SPR* reflectance imaging. Total five proposed uses of *SPR* reflectance imaging technique are presented: (1) micromixing concentration field development of ethanol penetrating into water contained in a micro-channel, (2) full-field detection of the near-wall salinity profiles for convective/diffusion of saline droplet into water, (3) full-field and real-time surface plasmon resonance imaging thermometry, (4) correlation of near-field refractive index of nanofluids with surface plasmon resonance reflectance, and (5) unveiling hidden complex cavities formed during nanocrystalline self-assembly.

Keywords: Surface Plasmon Resonance (*SPR*), Transport properties, Micro/nano fluidics, Concentration, Salinity, Temperature, Hidden cavity, Nanoparticles, Effective Refractive Index, TIR, Evanescence

TABLE OF CONTENTS

CHAPTER 1 Introduction **1**

1.1 Surface Plasmon Resonance (*SPR*) **1**
1.2 Motivation and Objectives **4**
1.3 Organization of the Study **4**

CHAPTER 2 Fundamentals of *SPR* **6**
2.1 Principle of *SPR* **6**
2.2 Governing Equation **8**
2.3 Modified Drude Model **10**
2.4 Spatial and Line of Sight Resolutions **13**
2.5 Penetration Depth of Surface Plasmon Wave **14**

CHAPTER 3 Proposed Uses of *SPR* Reflectance Imaging **16**
3.1 Micromixing Concentration Profiles of Binary Liquids **16**
3.2 Near-Wall Convective/Diffusive Saline Concentration Profiles **31**
3.3 Full-Field and Real-Time *SPR* Imaging Thermometry **40**
3.4 Correlation of Near-Field Refractive Index of Nanofluids with Surface Plasmon Resonance Reflectance **48**
3.5 Unveiling Hidden Complex Cavities Formed during Nanocrystalline Self-Assembly **55**

CHAPTER 4 Conclusion **66**

REFERENCES **67**

APPENDIX **77**

VITA **80**

LIST OF TABLES

2.1	Parametric values for the calculation of the temperature dependent thin metal refractive indices	11
3.1	Thermophysical and optical properties of ethanol and water	18
3.2	Measurement uncertainties for *SPR* reflectance *R* and its six individual contributions	28
3.3	Measurement uncertainties for *SPR* reflectance *R* and its three individual contributions	39

LIST OF FIGURES

1.1	Schematic *SPR* and *TIR* principle.	2
2.1	Kretschmann configuration of a three-layered *SPR* principle.	7
2.2	Effect of temperature dependency of thin metal film on *SPR* reflectance thermometry	12
2.3	Lateral resolution of *SPR* imaging as a function of ethanol mass concentration in water based on the *SPR* decay length.	14
3.1	Experimental layout of the *SPR* imaging system using a *p*-polarized white light source.	17
3.2	Calculated *SPR* reflectance as functions of the incident angles for different ethanol mass concentrations.	19
3.3	Dependence of *SPR* reflectance *R* and the test field refractive index *n* on the ethanol concentration in water.	20
3.4	Calibration results of the normalized pixel gray levels.	22
3.5	Full-field development of ethanol mixture concentrations penetrating into water contained in a microchannel.	23
3.6	Temporal development (30 ms ~ 300 ms) of ethanol concentration distributions along the channel centerline in two different spatial measurement resolutions.	25
3.7	The normalized uncertainty for *SPR* reflectance (ω_R / R) as a function of ethanol concentration.	29
3.8	*SPR* reflectance and calibration for salinity.	33, 34
3.9	Full-field and real-time mapping of near wall salinity when a 0.8-mm diameter drop with 10% saline mass concentration is dropped into 3-mm thick pure water.	36, 37
3.10	*SPR* reflectance *R* as functions of water temperature seven different prism materials using the dielectric constant of Kolomenskii for a thin Au film of 47.5 nm thickness.	42
3.11	*SPR* reflectance *R* as functions of water temperature for seven different refractive index values measured for thin metal films of approximately 47.5 nm thickness, coated on the top surface of a BK 7 prism.	44
3.12	Full-field and real-time mapping of transient temperature fields when a hot water droplet (80°C) falls on the cold Au surface (20°C) in (a) air environment and (b) water environment.	46
3.13	Experimental determination of effective refractive index (ERI) of nanofluids containing 47 nm Al_2O_3 nanoaprticles using total internal reflection (*TIR*) technique.	49
3.14	A schematic illustration of *SPR* reflectance imaging, and a correlation of *TIR*-measured ERI of nanofluids (47 nm Al_2O_3) with normalized *SPR* reflectance *R* for different loadings.	52
3.15	Full-field and real-time mapping of ERI and volume concentration distributions of evaporating nanofluid containing 47 nm Al_2O_3	54

nanoparticles.
3.16 Simultaneous imaging of microscopic dorsal view from the top, near-field *SPR* fingerprinting, and natural fringe ventral view of the crystallized inner cavity structure. 57
3.17 The *SPR* fingerprinting identifies the existence and layout of hidden cavity structures by distinguishing *s-l-g* phase regions. 59
3.18 Anatomy of a self-assembled nanocrystalline structure revealing the hidden hollow complex cavities. 62, 63

CHAPTER 1
Introduction

1.1 Surface Plasmon Resonance (*SPR*)

The use of foreign trace particles, such as fluorescence dyes or liquid crystal particles [1], in measuring fluidic concentrations and temperature fields can alter the flow properties because of the physical and dynamical intrusiveness by themselves. The level of the experimental bias will be more substantial for microscale experiments because of the increased intrusiveness with decreasing length scales. Label-free imaging, therefore, is desirable to provide more accurate examination of microfluidic and thermal fields.

Of the many techniques that have been examined for the purpose of measuring microfluidic and thermal fields—including differential interference contrast (*DIC*) imaging, dark-field imaging, phase contrast imaging, shearing interferometry [2] and reflected light microscopy techniques, and detecting temperature fileds-including thermocouple (*TC*), and laser induced fluorescence (*LIF*) [3], surface plasmon resonance (*SPR*) reflectance variation is considered to be most sensitive, label-free, full-field and real-time detection tool to visualize the refractive index of a mixture and the variation of temperature fields.

The evanescent wave field of total internal reflection (*TIR*) is amplified along the interface between the noble metal (Ag, Au, Cu, Al) film layer and the test fluid (Fig. 1.1a) [4,5]. When the p-polarization wave-vector of the *TIR* light matches the surface plasmon wave vector at a certain incident angle, called the *SPR* angle, SP excitation and amplification occur (Fig. 1.1b). This phenomenon is called Surface Plasmon Resonance (*SPR*) [6,7]. The history about *SPR* phenomena is well described in reference [6]. In return, the intensity of the *TIR* light is greatly reduced as most of the incoming photons are converted to the electron energy of SP waves entering the thin metal film and exiting as amplified *SPR*. The magnitude of the p-polarized *SPR* reflectance is extremely sensitive to the refractive index variation of the near-wall fluid region above the thin metal layer. Note that s-polarization wave-vector is not subjected to *SPR* and is totally

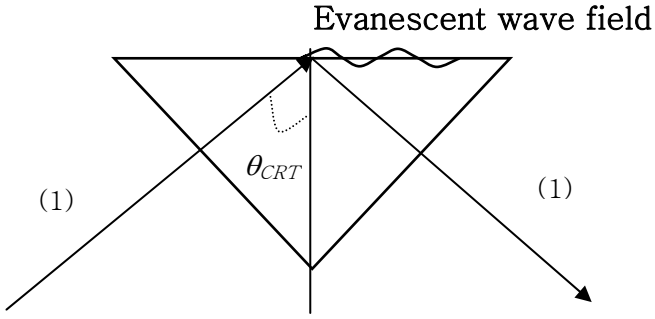

(a) Total Internal Reflection [4,5]

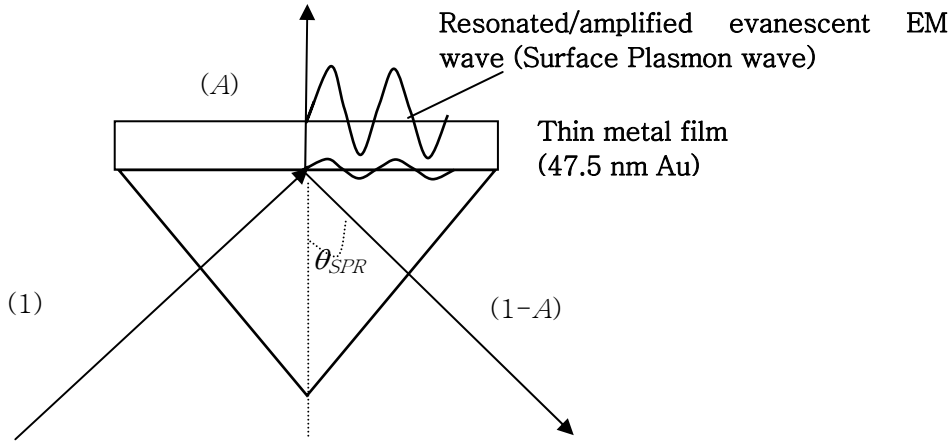

(b) Surface Plasmon Resonance Reflection [7]

Figure 1.1 Schematic *SPR* and *TIR* principle. Detail explanation for *SPR* configuration is described in Fig. 2.1.

reflected.

Various techniques using the *SPR* principle are currently applied to research, which is rapidly expanding to comprise a variety of interests, including biochemical, biomedical, pharmaceutical, chemistry, polymer and various other engineering fields. One of the most active areas of research is in the field of biomedicine, which is exploring protein-protein interactions, substrate-DNA/cell/protein/enzyme joining, receptor-ligand attractions, and a number of other applications of timely importance [7-17]. Other essential applications outside the field of biomedicine include measurements of thin polymer film thicknesses [18-21], the sensing of specific gas or liquid components [22-25], point-wise temperature measurements, theoretical modeling for hydrogenated amorphous silicon, silver film, titanium dioxide layer (TiO_2), a mixture of ethanol and glycol [22, 26-28] and the nanoscale optics in the near and wide field using localized surface plasmon polarization [29-33]. In addition, diverse techniques are presently being developed and tested using the surface plasmon optical characteristics: classical *SPR* [14, 34,35], *SPR* interferometry [36-38], SP coupled emission [6,39], *SP* fluorescence spectroscopy [8, 9,40,41], *SPR* microscopy [42-44], nano-optics of SP polarization [29-33], and *SPR* scattering of nanoparticles [45,46].

However, the advantageous merits of *SPR* sensing, based on the *SPR* reflectance, have not been explored as a full-field detection tool for near-field transport properties in micro/nanoscale fluidic phenomena. Traditionally, *SPR* microscopy has been used in diverse applications. Rothenhausler and Knoll [44] and Berger et al. [42] presented full-field images of thin film thickness changes by detecting the *SPR* reflectance variation depending on the film thickness. Brockman et al. [43] and Lee et al. [10] suggested the detection of multiple DNA array interactions by measuring the multiple point-wise *SPR* reflectance information with time. Lam et al. [23] showed the point-wise detection of a binary mixture (glucose and water) concentration with *SPR*. Fu et al. [47] used the wavelength-tunable *SPR* microscopy to detect the point-wise changes of refractive index of saline solution. None of these results, however, provide measurements of concentration distributions in full-field and real-time nature. Zhang et al. [38] showed three-dimensional imaging of the dynamic process of alcohol using the *SPR*

interferometric method. While their method analyzes the interferogram to obtain refractive index variations, this analysis is not applied directly to concentration field distribution. Menguc's group showed that *SPR* phenomena are utilized to characterize the scattering of nanosized particles, with the parameters of size, shape, and orientations of these particles [45,46].

In this study, a label-free, full-field and real-time quantitative visualization technique using the *SPR* reflectance imaging is presented as a new optical tool to nonintrusively measure the near-field transport properties in micro/nanoscale fluidic phenomena.

1.2 Motivation and Objective

Originally, this study starts from the trial to visualize the concentration profile of transparent binary liquids in a label-free, real-time and full-field manner. Foreign materials can affect or alter transport properties of test medium and cause measurement inaccuracy. To overcome this problem, non-intrusive label-free technique is investigated in this study. Most techniques such as enhanced microscopy and interference do not work through several trial and errors except *SPR* technique. *SPR* is known to be highly sensitive to the variation of refractive index of test medium with 10^{-8} in refractive index (RI) unit [48] because the electric field of surface plasmon is dramatically enhanced near the interface between metal thin film and test medium. For this reason, *SPR* is employed as a sensing platform for a label-free mapping of transport properties of micro/nanoscale fluidic phenomena. For the first time, surface Plasmon resonance (*SPR*) reflectance imaging technique is implemented and applied in the field of thermal-fluids to detect transport properties such as concentration, temperature, salinity, hidden cavities, and effective refractive index in a label-free, real-time, and full-field manner. This study aims to develop *SPR* reflectance imaging technique and demonstrate its applications to detect transport properties of micro/nano fluidic phenomena.

1.3 Organization of the Study

This study consists of development of surface Plasmon resonance (*SPR*)

reflectance imaging technique for label-free mapping of transport properties in micro/nano fluidic phenomena and its five practical applications. Chapter 2 describes the fundamentals of *SPR* covering its principle, governing equation, modified Drude model for the consideration of temperature effect of metal film, and the resolution. Chapter 3 shows the proposed uses of *SPR* reflectance imaging technique in five applications. Section 3.1 presents a visualization of micromixing concentration profiles of binary liquids when a drop of ethanol propagates to pure water stored in microchannel by capillary phoretic suction force. Section 3.2 shows a detection of transient near-wall convective/diffusive salinity profiles when a droplet of saline solution is dropped into pure water on top of gold thin film surface to show the formation of vortex ring in the shape of “donut”. Section 3.3 demonstrates the possibility of *SPR* thermometry based on modified Drude model to detect the temperature field in real-time and label-free when hot water droplet is put in the test medium of air or cold water. Section 3.4 discusses the unveiling of hidden hollow cavities formed during evaporative nanocrystalline structure self-assembly by using *SPR* near-field imaging and natural fringe mapping technique with digital fringe analysis. Dramatic and scientifically meaningful finding is observed using *SPR* near-field mapping technique. Section 3.5 presents the correlation of refractive index of nanofluids with surface plasmon resonance technique to show that effective refractive index of nanofluids is linearly dependent on volume fraction of 47 nm Al_2O_3 nanofluids. Chapter 4 is the conclusions derived from this study and provides recommendations for further research.

CHAPTER 2

Fundamentals of *SPR*

2.1 Principle of *SPR*

The *SPR* technique is known for its high sensitivity in measuring refractive index variations on the order of 10^{-8} sensitivity [48]. In addition, the illuminating intensity of the *SPR* wave is about 10 times greater than the ordinary evanescent wave field generated by the total internal reflection (*TIR*) under the same illumination source strength [9, 40, 41).

Figure 1.1 illustrates the very basic concept of *SPR* reflectance and an experimental schematic as a real-time and full-field refractive index imaging tool. When the incident ray exceeds a critical angle onto the prism interface (Fig. 1.1a), the intensity of the total internal reflection remains identical to that of the incident ray, while the evanescent light wave field is created to quickly decay within a few hundred nanometers, from the interface [4,5]. When the prism interface is coated with a thin metal (Au) layer (Fig. 1.1b), the evanescent EM field induces the abundant free electrons to oscillate and resonate at an optimized PR condition. The resulting resonated and amplified evanescent wave field is created along the top surface of the metal layer. Because of the absorption by resonance of the incident ray, the reflectance intensity is reduced by the amount of resonant absorption (A), and the absorption amount directly depends on the refractive index of the test fluid contacting the thin metal film when other optical conditions are fixed. In turn, the refractive index of test medium depends on the local concentrations or temperatures.

Figure 2.1 schematically illustrates the Kreschtmann's principle of *SPR* occurring at the interface of a thin-layered metal film contacting the external test medium [34]. When a thin metal film is illuminated by a coherent p-polarized light at an incident angle exceeding the critical angle for total internal reflection, the evanescent wave vector ($\vec{k}_x$) is formed at the incident (bottom) metal surface that successively triggers coherent fluctuations of free electrons at the surface of the metal film [49]. This coherent energy conversion of the photons into free electrons is called the Surface Plasmon (*SP*)

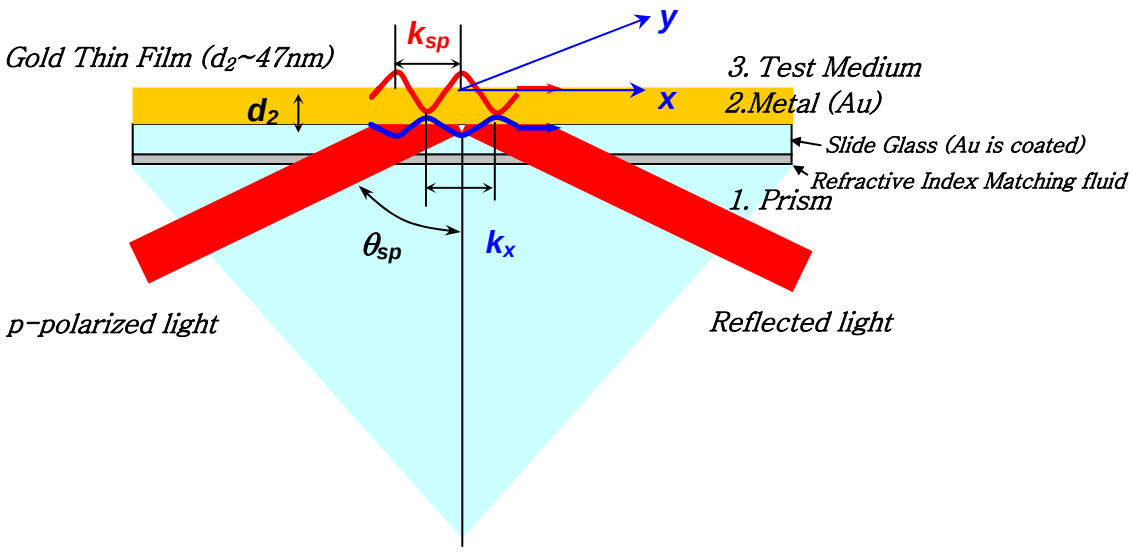

Figure 2.1 Kreschmann configuration of a three-layered *SPR* principle consisting of the glass prism (1), the metallic gold film (2), and the test medium (3), where θ_{sp} is the surface plasmon angle, d_2 is the thickness of the gold film, k_x denotes the wave propagation number of the evanescent wave, and k_{sp} denotes the wave propagation number of the *SPR* wave. In most experiments, thin metal film is coated on slide glass which is placed on top of prism using refractive index matching fluid, and this layer of refractive index matching fluid is neglected in Fresnel calculation [58,59].

phenomenon. The resonant excitation of SP in the laterally heterogeneous interface occurs when the condition of momentum matching is fullfilled, i.e., $\vec{k}_x = \vec{k}_{sp}$ where $\vec{k}_x$ is the evanescent wave vector along the surface. When the SP waves penetrate into the very thin metal film and collectively oscillate to form amplified waves, the *SPR* wave is achieved on the emitting (top) surface of the metal layer [6,9].

As a result of the *SPR* excitation and absorption of the incident light into the metal film, the reflected light intensity is darkened and is ideally nullified at the specified SP angle [44]. The parameters determining the SP angle include the incident light wavelength, the type and thickness of the metal film, refractive index values of the metal layer and the prism, and the refractive index of the test medium. Thus, once the SP angle is set for the base fluid at reference concentration or temperature with the specified conditions showing the darkest background image, any local changes of refractive index distribution in the test field as the result of mixing with secondary fluid or variations of temperature will reduce the local *SPR* absorption and enhance the corresponding *SPR* reflectance. This is the key idea to non-intrusively detecting the concentration fields of a binary mixture or the temperature fields with fine spatial measurement resolution and high accuracy.

The *SPR* excitation requires specific conditions for metal properties in that the real part of its dielectric constant must be negative and its absolute magnitude greater than that of the imaginary part [9, 50]. There are several noble metals available for *SPR* applications, including silver, gold, copper and aluminum. Among them, gold is preferred because of its stability and superior performance in various environmental conditions.

2.2 Governing Equation

The *SPR* reflectance R based on the three-layer configuration (Fig. 2.1) is regarded as a function of related optical and geometrical parameters as:

$$R = R\left(n_1, n_2, n_3, d_2, \lambda_I, \theta\right) \qquad (2.1)$$

where n is refractive index, d is the gold layer thickness, λ_I is the incident wave length, and θ is the incident ray angle. The subscripts i = 1, 2, and 3 refer to prism, thin film metal, and test medium, respectively.

Fresnel equations relating p-polarization [4,51] gives:

$$R = |r_p|^2 \qquad (2.2)$$

$$r_p = \frac{[r_{12} + r_{23}\exp(2ik_{z2}d_2)]}{[1 + r_{12}r_{23}\exp(2ik_{z2}d_2)]} \qquad (2.3)$$

$$r_{12} = \frac{(Z_2 - Z_1)}{(Z_2 + Z_1)}, r_{23} = \frac{Z_3 - Z_2}{Z_3 + Z_2} \qquad (2.4)$$

$$Z_i = \frac{\varepsilon_i}{k_{zi}}, k_{zi} = [\varepsilon_i(\omega/c)^2 - k_{x1}^2]^{0.5}, i = 1,2,3 \qquad (2.5)$$

$$k_{x1} = \omega / c \sin\theta \varepsilon_1^{1/2} \qquad (2.6)$$

where r_p is reflection coefficient, ω is the angular frequency of incident ray, c is the speed of light, k is the wave number, ($k^2 = k_x^2 + k_z^2$), equivalently the magnitude of the wave vector $\vec{k}$, and ε is the dielectric constant. The dielectric constant of liquid is obtained from the relationship $\varepsilon = n^2$ [9].

Computational calculations by setting R = 0 in Eq. (2.2) predict the optimum incident angles for zero reflectance as 43.5° for air test medium, 70.7° for water test medium, and 74.9° for ethanol test medium, when d_2 = 47.5-nm gold layer is illuminated by 632.8-nm waves at 20°C through a BK7 glass prism (n1 = 1.515). For the case of a thicker or thinner film than the optimum 47.5 nm, less of the evanescent wave is absorbed or transmitted through the film to amplify the resonance, and, in turn, the *SPR* reflectance increases. All fluid temperatures (air, water, ethanol) remain constant at 20°C in the temperature-controlled laboratory environment, with estimated maximum uncertainties of ±0.5°C.

2.3 Modified Drude Model

To consider the temperature effect on metal film dielectric constant, the modified Drude model is incorporated in the Fresnel equation. The dielectric constant of thin metal film is given by Drude model [26,27,52,53] as:

$$\varepsilon \equiv (n_r + in_i)^2 = 1 - \frac{\omega_p^2}{\omega(\omega + i\omega_c)} \qquad (2.7)$$

where ε, n_r, n_i are the dielectric constant, the real and imaginary parts of thin metal film refractive index, respectively. ω is the angular frequency of the illuminating light, and ω_p and ω_c are the plasmon frequency and the collision frequency of thin metal film, respectively. Eq. (2.7) is expanded to provide

$$n_r^2 - n_i^2 = 1 - \frac{\omega_p^2}{\omega^2 + \omega_c^2}, \; 2n_r n_i = \frac{\omega_c \omega_p^2}{\omega(\omega^2 + \omega_c^2)} \qquad (2.8)$$

The plasma frequency is defined as [4]:

$$\omega_p = \sqrt{\frac{4\pi N e^2}{m^*}} \qquad (2.9)$$

where N and m^* are the free electron number density and effective mass of a single electron, respectively. The temperature dependence of ω_p is given as [26,52]:

$$\omega_p = \omega_{p0}[1 + \gamma_e (T - T_0)]^{-1/2} \qquad (2.10)$$

where γ_e is the thermal volume expansion coefficient of thin metal film and T_0 is the reference temperature (90°C for the present case). It is shown that the temperature dependence of ω_p is negligibly small compared with that of ω_c [52], and thus, only the

latter will be retained in determining the temperature dependence of the thin metal film dielectric constant in Eq. (2.8).

The collision frequency ω_c consists of phonon-electron scattering frequency ω_{cp} and electron-electron scattering frequency ω_{ce} [26,27,52], i.e.,

$$\omega_c = \omega_{cp} + \omega_{ce}$$
$$\omega_{cp}(T) = \omega_0[(\frac{2}{5} + 4(\frac{T}{T_D})^5 \int_0^{T_D/T} \frac{z^4}{e^z - 1} dz \qquad (2.11)$$
$$\omega_{ce}(T) = \frac{1}{6}\pi^4 \frac{\Gamma\Delta}{hE_F}[(k_B T)^2 + (\frac{h\omega}{4\pi^2})^2]$$

where all the constants and coefficients are listed in Table 2.1.

Using the experimentally determined refractive index $n = n_r + in_i = 0.1718 + i3.637$ for the 47.5 nm Au thin film at the incident wave length of 632.8 nm [54], Eq. (2.10) is solved to determine $\omega_p = 3.7826\omega$, and $\omega_c = 0.08802\omega$ where the specified $\omega = 2\pi c/\lambda$ = 2.9788 X 10^{12}rad/s. Substituting these results into Eq. (2.11) gives ω_0 = 1.171 X 10^{14} *rad/s*.

The *SPR* curve accounting for the temperature variation effect in Fig. 2.2 is determined from the aforementioned analysis and calculations. Two parameters of thermal expansion and dielectric constant are considered to investigate the temperature

Table 2.1 Parametric values for the calculation of the temperature dependent thin metal refractive indices

Symbols	Description	Value
T_D	Debye temperature	170 K
E_F	Fermi energy	5.53 eV
k_B	Boltzmann's constant	1.3807 × 10-^{23} J/K
Γ	Scattering probability	0.55
Δ	Fractional umklapp scattering	0.77
h	Plank constant	1.0546 X 10^{-34} Js

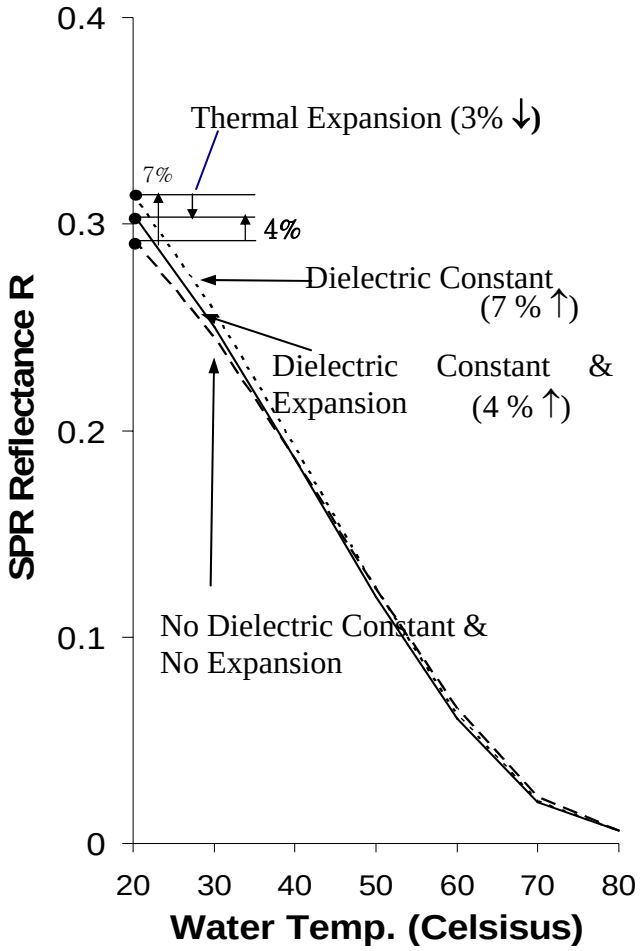

Figure 2.2 Effect of temperature dependency of thin metal film on *SPR* reflectance thermometry (Dielectric constant & thermal expansion).

effect on *SPR* reflectance imaging thermometry. The thermal expansion factor has the 3% decrease effect and the dielectric constant has the effect of 7% increase effect. On average, the temperature variation consideration has the 4% increase effect.

2.4 Spatial and Line of Sight Resolutions

Because of the plane wave optical components, the lateral resolution of *SPR* imaging, as in normal wide-field light microscopy, is affected by the well-known diffraction limit length scale, $l_{\min} = 1.22\lambda f / D$ [44], also referred to as a Rayleigh criterion [4].

In addition, SP waves occur in a propagating mode and are strongly damped in their direction due to intrinsic dissipation [55,56] and radiative damping [35,57]. The propagation length that a surface plasmon wave travels along the interface, between the test medium and the gold thin film, is defined by decay length L_x [42,44]. The decay length, or equivalently, the distance along the surface where the attenuation of the plasmon field occurs is proportional to 1/e, the reciprocal of an exponential function, or equivalently to, $L_x = \frac{1}{2k_{sp}''}$, where k_{sp}'' is the imaginary part of the surface plasmon wave vector along the surface, i.e., $k_{sp} = k_{sp}' + ik_{sp}'' = \frac{2\pi}{\lambda}(\frac{\varepsilon_2\varepsilon_3}{\varepsilon_2+\varepsilon_3})^{1/2}$.

The calculated decay length L_x as a function of ethanol concentration is shown in Fig. 2.3, where the upper and lower limits refer to the elementary uncertainties of λ, ε_2 and ε_3 for the test medium of water/ethanol binary liquids (The following section includes more detailed discussions on measurement uncertainties in Chapter 3, see Table 3.2) The lateral resolution is approximately 4.5 μm for all tested ethanol concentrations and is approximately equivalent to seven pixels of the CCD camera, with each pixel covering a 0.66-μm square in the physical domain.

The line-of-sight resolution of *SPR* imaging is estimated to be in the order of one nanometer based on the resonance contrast, while the line-of-sight resolution for normal wide-field light microscopy is typically in the order of 10 nm based on the interference

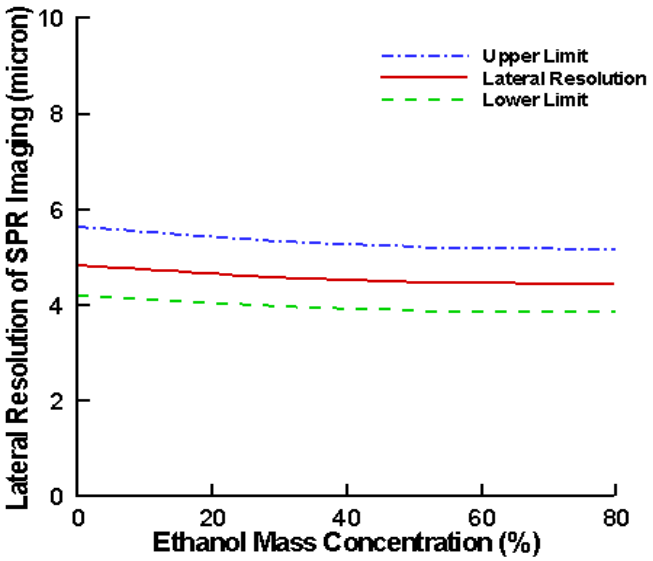

Figure 2.3 Lateral resolution of *SPR* imaging as a function of ethanol mass concentration in water based on the *SPR* decay length [58,60].

contrast [42,44]. Thus, the *SPR* technique can provide additional benefits in accurately measuring thin film thicknesses [18-21] or the separation distance between two interfaces [8,17] with substantially enhanced accuracy.

SPR technique can provide additional benefits in accurately measuring thin film thicknesses [18-21] or the separation distance between two interfaces [8,17] with substantially enhanced accuracy.

2.5 Penetration Depth of Surface Plasmon Wave

Surface Plasmon wave has the evanescent characteristics, and its penetration depth (δ) or skin depth is defined as the depth at which the electric field of evanescent surface plasmon wave falls to 1/e from dispersion relationship [6];

$$\delta = \frac{1}{|k_{zi}|}$$

$$for\ \ test\ \ medium\ \ , \delta = \left| \frac{\lambda}{2\pi} \left(\frac{\varepsilon_2^{'} + \varepsilon_3}{\varepsilon_3^2} \right)^{1/2} \right| \qquad (2.12)$$

$$for\ \ metal\ \ \ film\ , \delta = \left| \frac{\lambda}{2\pi} \left(\frac{\varepsilon_2^{'} + \varepsilon_3}{\varepsilon_3^{'2}} \right)^{1/2} \right|$$

where ε_2 and ε_3 are dielectric constants of metal film and test medium, respectively. ε_2' is real part of ε_2. Penetration depth, δ is a function of incoming light wavelength, and dielectric constants of test medium and metal film. In the case of λ=632.8 nm, gold (ε_m=*-13.2+1.25i*), and test medium of water or air, penetration depth is calculated as;

for test medium side, δ = 192 nm for water and 353 nm for air, and for metal side, δ = 25 nm for water and 26 nm for air. While the penetration depth for total internal reflection (*TIR*) is given as [4,5]

$$\delta_{TIR} = \frac{\lambda}{4\pi\sqrt{(NA^2 - n_3^2)}} \qquad (2.13)$$
$$NA = n_p \sin(\theta_i)$$

where n_p is refractive index of prism, *NA* is numerical aperture, θ_i is incident angle of incoming light. Penetration depth δ_{TIR} is calculated as *95 nm* for water and *49 nm* for air, respectively with λ=632.8 nm, prism of SF 10 (n_p=*1.723*), and the incident angle of 56.3 degree for the *SPR* optimum angle ofpure water (n=1.3321), while critical angle θ_c=$sin^{-1}(n_t/n_p)$= sin^{-1}*(1 and 1.3321 / 1.723) = 35.5 and 50.6 degree* for air and water, respectively.

CHAPTER 3

Proposed Uses of *SPR* Reflectance Imaging

3.1 Micromixing Concentration Profiles of Binary liquids

3.1.1 Experimental Methods

Figure 3.1 shows the optical arrangement of the *SPR* imaging system that was designed and constructed at the University of Tennessee. The present experimental set-up uses white light source that is monochromatized by a narrow bandpass filter [43,44]. The randomly polarized white light from a 100-watt Tungsten-Halogen lamp collimates onto the p-polarizer to provide only p-polarization light, the E-field of which is parallel to the incident plane. The rotating mirror adjusts the incident angle to the optimized SP angle, and the incident ray illuminates onto the gold film of 47.5-nm nominal thickness that is laid on the 2.5-nm thick Titanium adhesion layer coated on the 0.16-mm thick cover glass substrate. The gold-coated substrate is then attached to the prism (BK7 glass with n = 1.515) using index matching fluid (n = 1.515, Newport Inc.) to fill the micro-gap in-between.

A rectangular microchannel with a cross-section of 50-μm (h) x 91-μm (w) is constructed directly on the top surface of the gold film. Two pieces of 50-μm thick self-adhesive plastic tape are placed with 91-μm separation, and a glass slip cover is placed on top to complete the rectangular channel configuration.

The band pass filter narrows the white light spectra to the center at 632.8-nm, with its full width half maximum (FWHM) of 10-nm. Sony XC-75 CCD (640 x 480 pixel resolution) uses a long focal distance lens of Mitutoyo M Plan Apo 5x (NA = 0.14 f = 40 mm) to record microscale *SPR* images of the near-field test region.

The *SPR* intensity at the SP angle should be nearly zero, showing a dark background image when the test region is filled entirely by the base fluid of water. When the second fluid, ethanol, penetrates into the base fluid, the local index of refraction changes (Table 3.1), and the aforementioned optimum SP conditions for zero reflection are not sustained. As a result, the mixed region will appear brighter than the dark background, and the brightness increases with increasing concentration of ethanol.

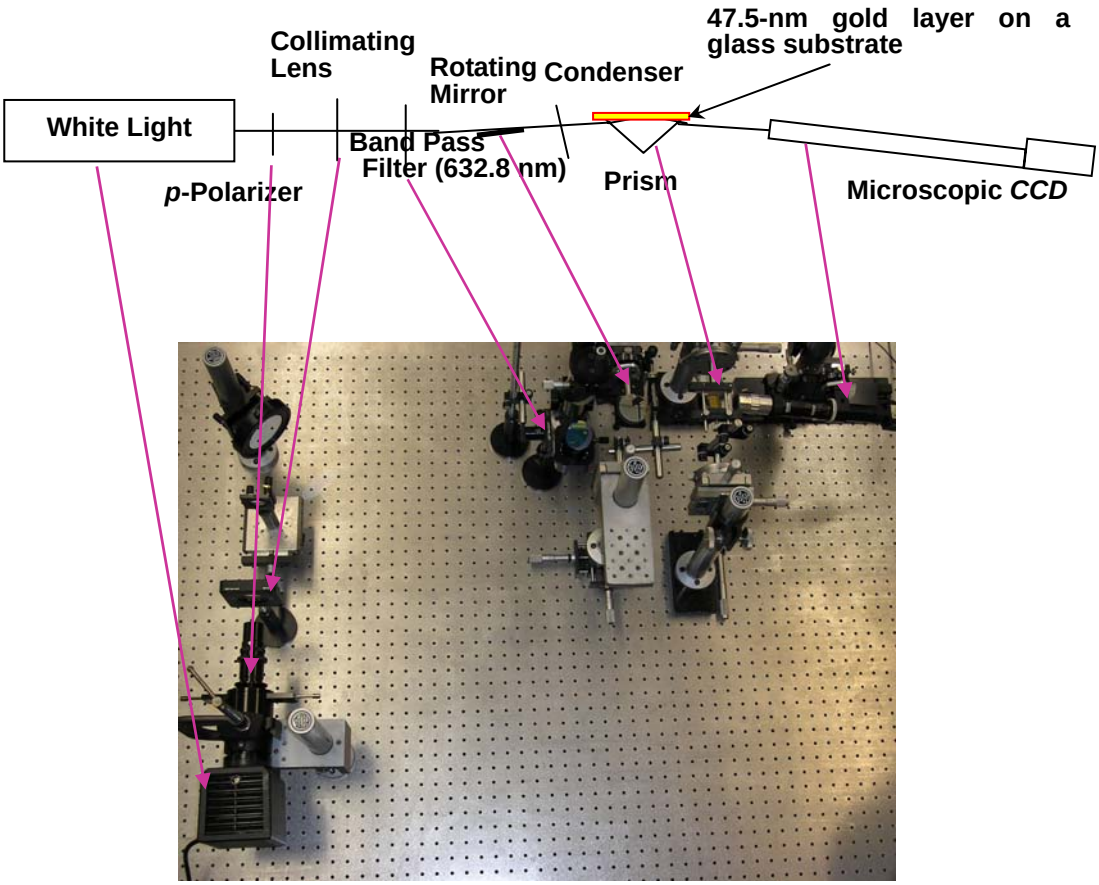

Figure 3.1 Experimental layout of the *SPR* imaging system using a *p*-polarized white light source [58,60].

Table 3.1 Thermophysical [61] and optical properties [62] of ethanol and

Div.	Density (g/cm3)	Refractive Index	Optimum *SPR* angle (degrees)	Surface Tension (mN/m)
Ethanol	0.7893	1.3604	74.9	21.97
Water	1.0	1.3321	70.7	71.99

Therefore, the gray levels of the *SPR* image will represent the mixture concentration distributions.

3.1.2 Calibration Correlation of *SPR* Reflectance Imaging

Figure 3.2 shows the calculated reflectance curves as functions of incident angles for different ethanol mass concentrations in percentile. The corresponding SP angles, as shown in the inset Table, progressively increase from 71.5° for 10% ethanol by mass to 75.6° for 80% ethanol by mass, then gradually decrease to 74.9° for 100% or pure ethanol; all concentration units in this paper is percent by mass.

In Fig. 3.3a, the *SPR* reflectance is shown in a direct correlation with the ethanol mass concentration and is equivalent to the reflectance variation along the vertical dashed line in Fig. 3.2. The symbols show discrete calculation points, and the smoothing spline curve fits the points nicely with the square correlation R^2 = 0.995; curve fitting tool in Mattlab 7 is applied for the calculations and R^2 is defined as the square of the correlation between the response values and the predicted response values. The reflectance increases with increasing ethanol concentrations up to 80% in mass and shows slight decrease thereafter. This decrease is consistent with the decreasing refractive index of the mixture [61] beyond 80% concentration, as shown in Fig. 3.3b. This implies that the current *SPR* imaging carries inherent limitations in measuring ethanol concentrations higher than 80% mass fraction in water. Furthermore, at concentrations higher than 50%, two different ethanol concentrations generate an identical *SPR* reflectance intensity level and the current technique will be subjected to ambiguity in determining concentrations higher than 50%. For the case of more or less uni-directionally increasing ethanol concentration fields, like the present mixing case, however, the ethanol concentrations up to 80% can be

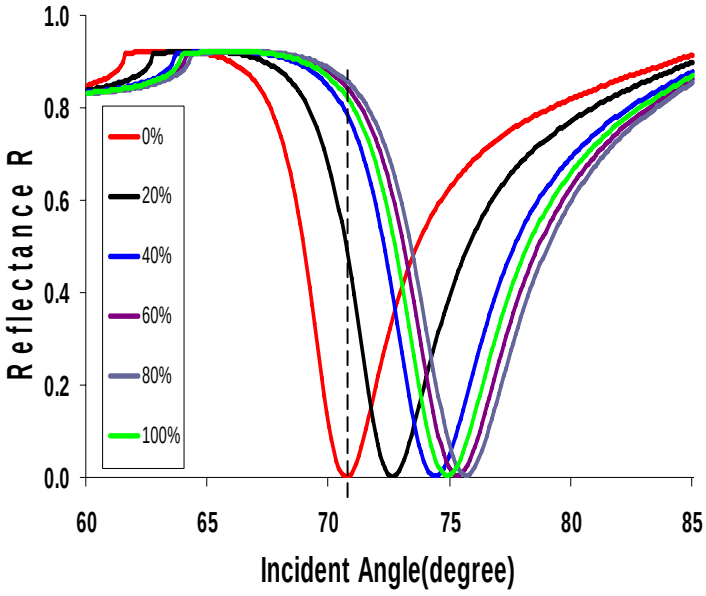

Ethanol concentration in water at 20°C (mass %)	*SPR* Angle (°)
0	**70.7**
10	71.5
20	72.6
30	73.6
40	74.3
50	74.9
60	75.2
70	75.5
80	**75.6**
90	75.5
100	74.9

Figure 3.2 Calculated *SPR* reflectance as functions of the incident angles for different ethanol mass concentrations in water: a BK7 glass prism (n_1 = 1.515) with 47.5-nm gold (Au) metal layer illuminated by *p*-polarized white light narrow-banded at 632.8 nm. The *SP* angles progressively increase from 70.7° for 0% ethanol, or pure water, to 75.6° for 80% ethanol, then gradually decrease to 74.9° for 100% or pure ethanol [58,60].

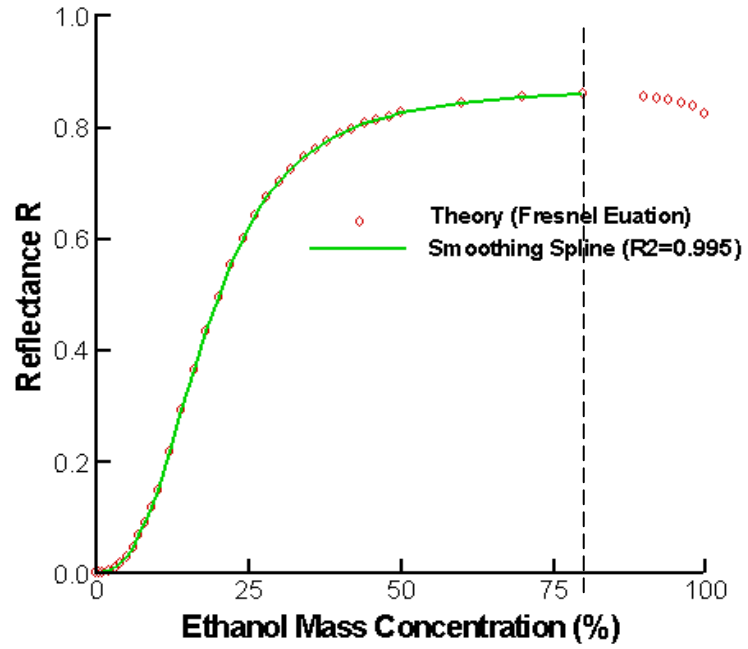

(a)

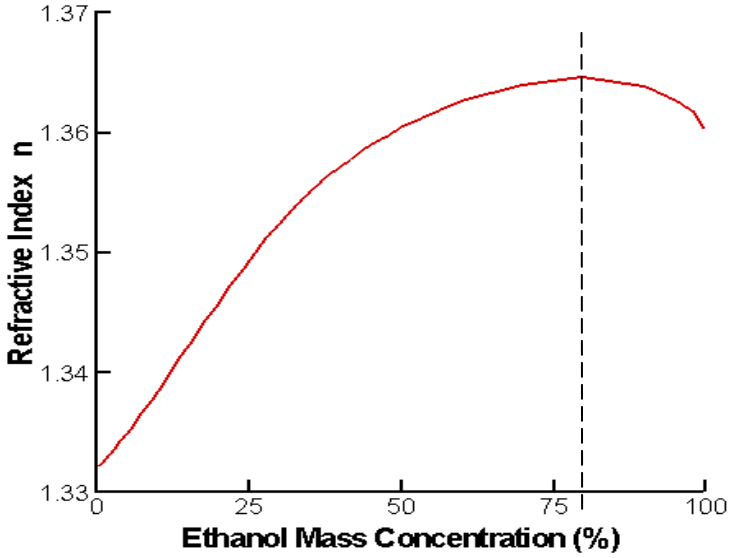

(b)

Figure 3.3 Dependence of *SPR* reflectance *R* and the test field refractive index *n* on the ethanol concentration in water: (a) The symbols represent calculated *SPR* reflectance using the three-layer Fresnel relationship of Eq. (2.2)-(2.6) and the solid curve represents the smoothing spline fitting with R^2 = 0.995, and (b) Refractive index variation of ethanol-water mixtures [61] (The *SPR* parametric conditions are identical to those of Fig. 3.2) [58,60].

examined since the *SPR* reflectance monotonically increases at least up to 80%. The reversing refractive index of ethanol/water mixture at high concentration range is attributed to the characteristics of ethanol/water molecular association and the aggregation of ethanol in water [63].

3.1.3 Results and Discussions

An initial calibration experiment is conducted to correlate the measured pixel gray levels of *SPR* images for nine specified ethanol/water mixtures with the reflectance curve fitting shown in Fig. 3.3a. In order to minimize the potential bias occurring from the background nonuniformities, as well as the pixel-to-pixel variation in the quantum efficiency, pixel-by-pixel correlations are facilitated individually for nine different mixture samples with specified ethanol concentrations ranging from 0 to 80% by mass. The highest measured pixel gray level, PGLmax, is set to the maximum *SPR* intensity at 80% ethanol concentration, and the lowest pixel gray level, PGLmin, is set to the *SPR* intensity at 0% or pure water.

Figure 3.4 shows the theoretical and experimental correlations of the ethanol mixture concentrations with the normalized pixel gray levels, defined as $(PGL - PGL_{\min})/(PGL_{\max} - PGL_{\min})$. The symbols show measured PGL data, and the error bars span the 95% confidence levels of uncertainties occurring from the individual 640x480 CCD pixels. The agreement of the calibration measurement data with the theory allows for the use of the predicted calibration curve to convert measured *SPR* image intensities into corresponding ethanol concentration values.

3.1.3.1 Ethanol Concentration Distributions Penetrating into Water in a Microchannel

Figure 3.5 shows the *SPR* images in pixel gray level contours (the left column) and the contour maps of the corresponding concentration distributions for the timely progress of ethanol penetrating from the left entrance into pure water filled in a microchannel. The primary drive for ethanol penetration into water is attributed to the capillary phoretic suction [64] by the small hydraulic radius of the micro-channel.

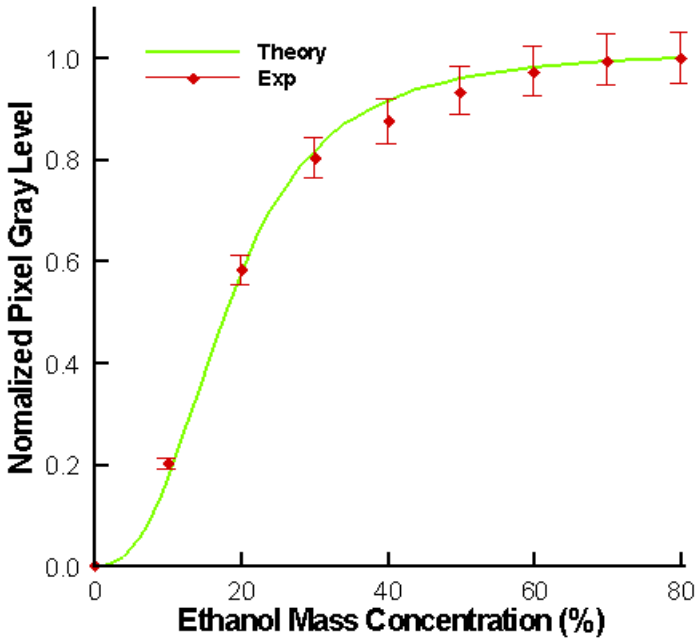

Figure 3.4 Calibration results of the normalized pixel gray levels ($\equiv (PGL - PGL_{\min})/(PGL_{\max} - PGL_{\min})$, where $PGL_{\min}$ and $PGL_{\max}$ correspond to pure water and 80% ethanol mixture, respectively) against the ethanol mass concentrations are shown by the symbols with the error bars of 95% confidence levels of the experimental data variation. Calculated correlations based on the Fresnel theory are shown by the solid curve [58,60].

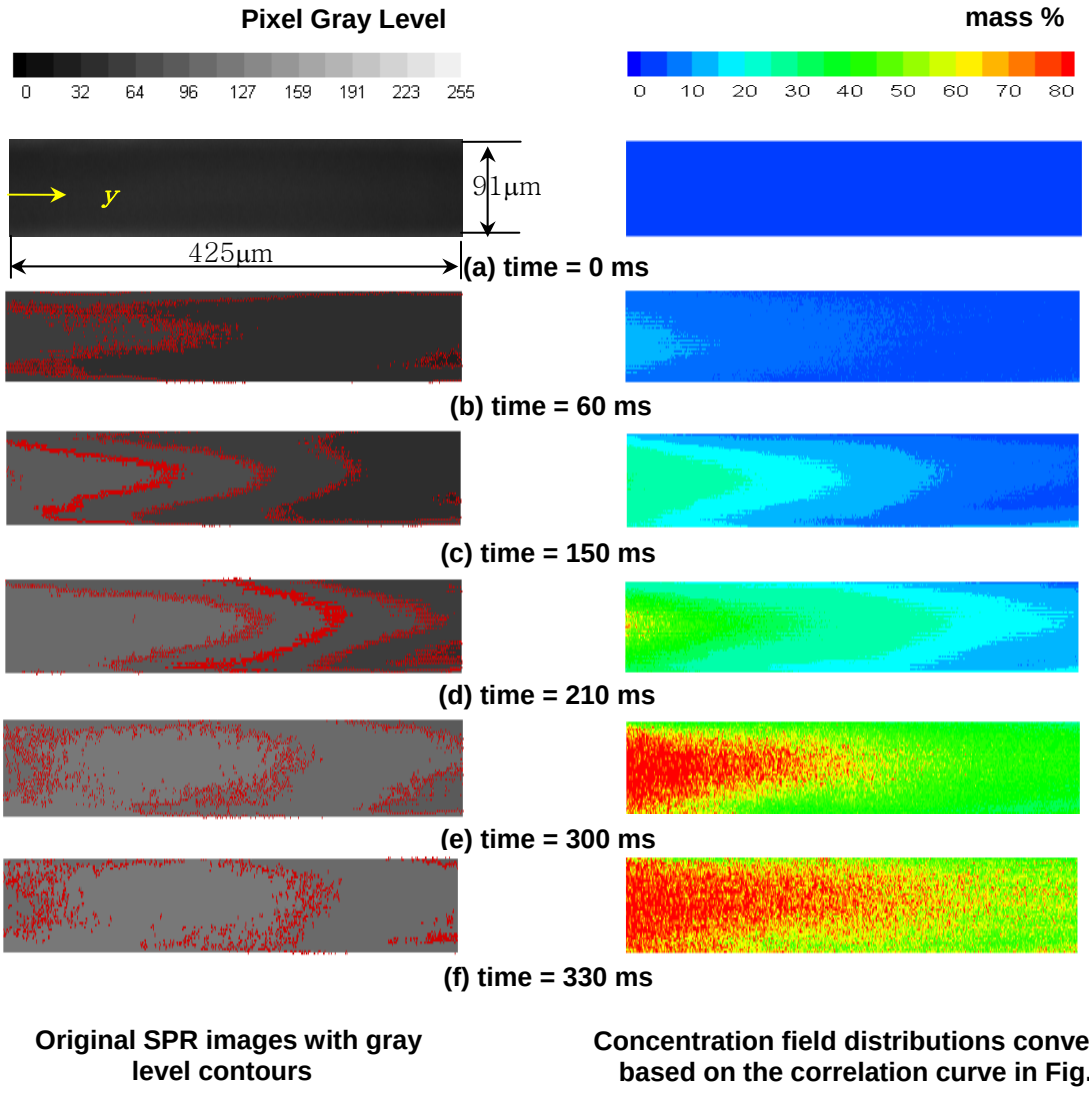

Figure 3.5 Full-field development of ethanol mixture concentrations penetrating into water contained in a microchannel (50-μm high and 91-μm wide) that drives a capillary phoresis rapidly from the left entrance to the right inside. Images represent the near-field region on the order of the penetration thickness of the evanescent wave field. The left column shows the recorded *SPR* images in gray level contours, and the right entrance (50-μm high & 91-μm wide). Thus, the ethanol-water interface rapidly advances to the right inside the channel. The ethanol-water interface is broadened because of the molecular diffusion progressively occurring during the interfacial advancement [58-60].

The *SPR* illumination wave field exponentially decays within a few hundred nanometers into the test field from the gold film surface, which is approximately consistent with the penetration depth of the evanescent wave field [65]. The *SPR* images shown in Fig. 3.5 represent the near-wall concentration fields confined within a thin fluid region of less than 1-μm spanning from the gold surface. This effective detection of the near-wall concentration field development is considered to be a unique advantage of the *SPR* imaging technique. For example, the near-wall concentration information will be very important in examining the viscous sublayer region for turbulent mixing process or determining the effect of slip boundary condition on mixing. The present shortcoming is that the maximum detectable ethanol concentration is limited to 80% because of the aforementioned *SPR* reflectance ambiguity, in that the reflectance increases with ethanol concentration up to 80% and then decreases thereafter.

Figure 3.6 shows the temporal development of ethanol concentration distributions along the channel centerline. A single-pixel of the *CCD* array is covering a 0.66-μm square in the physical field. Thus, 4-pixel binning of raw data (Fig. 3.6a) represents 2.64-μm square measurement spatial resolution, and 16-pixel binning (Fig. 3.6b) represents 10.56-μm resolution. The centerline ethanol concentrations show rapid increase with increasing time. At t = 300 ms, the ethanol concentrations near the channel entrance (for the case of 4-pixel binning) show saturation to 80%, which means that the local concentration can be anywhere from 80 to 100% ethanol in mass because of the inherent limitation of the technique associated with the ambiguity of the *SPR* reflectance versus ethanol concentrations as aforementioned in more details in the following section. The overall concentration profiles remain unchanged with the quadrupling of the binning order to 16-bit; however, the data fluctuations are substantially reduced at the cost of four-times coarse spatial data resolution. Nevertheless, the spatial resolution of 10.56-μm for the 16-bit binning is considered fairly acceptable for microscale concentration profile data resolutions. column shows the corresponding ethanol concentration distributions determined based on the calibration curve in Fig. 3.4.

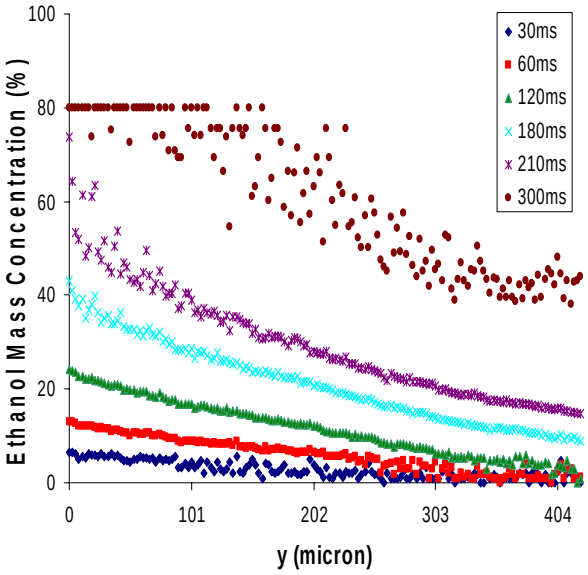

(a)

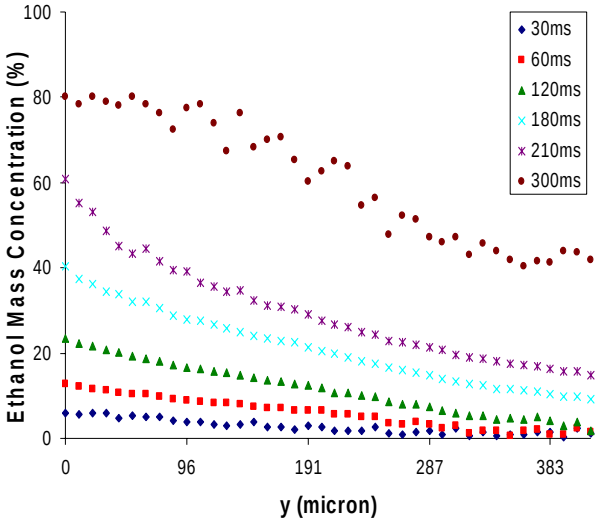

(b)

Figure 3.6 Temporal development (30 ms ~ 300 ms) of ethanol concentration distributions along the channel centerline in two different spatial measurement resolutions. Four (4)-pixel binning (a) provides 2.7-μm spatial resolution and shows saturations to 80% near the entrance, while more widely averaged results by 16-pixel binning with 10.6-μm spatial resolution (b) show less saturation at the cost of quadrupling the spatial resolution [58].

3.1.3.2 Measurement Uncertainty Evaluation

The uncertainty analysis is conducted based on the single point detection estimation given by Kline and McClintock [64]. The second-power equation referring to the measurement uncertainty of pixel gray level (*PGL*), which is linearly proportional to the reflectance *R*, is given as:

$$PGL \propto R = R(\varepsilon_1, \varepsilon_2, \varepsilon_3, d_2, \lambda_i, \theta, c) \tag{3.1}$$

$$\omega_R = \pm\left[\left(\frac{\partial R}{\partial \varepsilon_1}\omega_{\varepsilon_1}\right)^2 + \left(\frac{\partial R}{\partial \varepsilon_2}\omega_{\varepsilon_2}\right)^2 + \left(\frac{\partial R}{\partial \varepsilon_3}\omega_{\varepsilon_3}\right)^2 + \left(\frac{\partial R}{\partial \lambda_i}\omega_{\lambda_i}\right)^2 + \left(\frac{\partial R}{\partial \theta}\omega_{\theta}\right)^2 + \left(\frac{\partial R}{\partial d_2}\omega_{d_2}\right)^2 + \left(\frac{\partial R}{\partial c}\omega_c\right)^2\right]^{1/2}$$

where *R* is given as in Eq. (2.2), except that refractive index values are replaced by dielectric constants using $\varepsilon \equiv n^2$. The elementary uncertainties are estimated as:

$$\begin{aligned}
&\omega_{\varepsilon_1} = \varepsilon_1 \times 10^{-4} = \pm 2.296 \times 10^{-4},\ \omega_{\varepsilon_2} = \pm 0.0438 + \pm i0.148\ (\varepsilon_2 = -13.2 + i1.25),\\
&\omega_{\varepsilon_3} = \pm\varepsilon_3 \times 0.000025\ (\varepsilon_3 = n_3^2),\ \ \omega_{\lambda_i} = \pm 10\ nm,\ \omega_{\theta} = \pm 1/60^o = \pm 0.0167^o,\\
&\omega_{d_2} = 47.5\ nm \times 10\% = \pm 4.75\ nm,\ \omega_c = 0.01g
\end{aligned} \tag{3.2}$$

where the variation of the prism dielectric constant ω_{ε_1} is assumed negligible because of its extremely small variations of 10^{-4} or 0.01%. The elementary variations of dielectric constant of gold, ω_{ε_2}, are ±0.0438 and ±0.148 for its real and imaginary parts (The complex refractive index of gold film is given as $n_{\text{gold}} = 0.1718 + i3.637$), respectively [67]. The concentration of the nominal 100 % ethanol has 0.5% variation according to the manufacturer's specifications. The weighted factor of the variation is considered as the test medium uncertainties, which increase with increasing ethanol concentration. For example, for the test case of 40% ethanol concentration, 0.4*(0.5%) = ±0.2% is estimated for the elementary uncertainty ω_{ε_3}. The incident light wavelength variation is adopted from the narrow band pass filter specification with *FWHM* (Full-width half maximum) of 10 nm. The rotation stage that determines the incident angle has an accuracy of 1/60° = ±0.0167°. The thin film thickness uncertainty ω_{d_2} is estimated to ±10% as provided by the manufacturer (Playtypus Tech., *LLC*). The precision mass scale has a reading accuracy of 0.01g for mixing of ethanol and water.

The individual derivatives of R directly using Eq. (2.2) are too complicated to derive in their closed forms, primarily because of the coupling with complex refractive index of gold. Alternatively, numerical estimations for the derivatives have been conducted using the first-order finite differential scheme as follows:

$$\omega_R = \pm\left[\left(\frac{\partial R}{\partial \varepsilon_2}\omega_{\varepsilon_2}\right)^2 + \left(\frac{\partial R}{\partial \varepsilon_3}\omega_{\varepsilon_3}\right)^2 + \left(\frac{\partial R}{\partial \lambda_i}\omega_{\lambda_i}\right)^2 + \left(\frac{\partial R}{\partial \theta}\omega_{\theta}\right)^2 + \left(\frac{\partial R}{\partial d_2}\omega_{d_2}\right)^2 + \left(\frac{\partial R}{\partial c}\omega_{c}\right)^2\right]^{1/2} \quad (3.3)$$

$$\begin{array}{cccccc} : & : & : & : & : & : \\ (I) & (II) & (III) & (IV) & (V) & (VI) \end{array}$$

where each term represent an elementary uncertainty for the dielectric constant of gold thin film (I), the dielectric constant of test sample (II), the incident light wavelength (III), the incident angle (IV), the thin metal film thickness (V), and the mixing by mass scale (VI).

The differential ΔR in each elementary term is calculated for the range equivalent to the corresponding elementary uncertainty magnitude with respect to the specified test condition parameter. For example, for the case of term (III), $\Delta\lambda = \left[\lambda + \frac{\omega_\lambda}{2}\right] - \left[\lambda - \frac{\omega_\lambda}{2}\right]$ and $\Delta R = R(\lambda + \frac{\omega_\lambda}{2}; \varepsilon_2, \varepsilon_3, \theta, d_2) - R(\lambda - \frac{\omega_\lambda}{2}; \varepsilon_2, \varepsilon_3, \theta, d_2)$, where the test parameters are specified as λ = 632.8 nm and the elementary uncertainty is given as ω_λ = 10 nm. Note that all other parameters are taken as their test condition values, i.e., $\varepsilon_2 = -13.2 + i1.25$, ε_3 as specified for a given ethanol concentration, θ = 70.7°, and d_2 = 47.5nm.

Table 3.2 shows the summary results of uncertainty calculations, including magnitudes of the individual terms contributing in Eq. (3.3), for the range of ethanol concentrations from 10 to 80%, and Fig. 3.7a shows the normalized overall uncertainties ω_R / R corresponding to the last column of Table 3.2. The uncertainty of *SPR* reflectance is as high as ± 21.5% at 10% ethanol concentrations and dramatically decreases to less than ± 3.5% with increasing ethanol concentrations beyond 40%. In a stricter sense, the *CCD* camera detection accuracy of an order of 1 % [68] and the regression error of 0.5% for curve fitting (Fig. 3.3) should be accounted for in estimating

Table 3.2 Measurement uncertainties for *SPR* reflectance *R* and its six (6) individual contributions ($\varepsilon_2 = -13.2 + i1.25$, λ = 632.8 nm, θ = 70.7°, and d_2 = 47.5 nm)

Ethanol Concentration (Mass %)	Reflectance *R*	*Individual uncertainty terms in Eq.* (3.3) (x 10^4)						Overall Uncertainty ω_R	Normalized Uncertainty (= ω_R/R, %)
		I	*II*	*III*	*IV*	*V*	*VI*		
10	0.158	1.32	2.10	0.06	0.07	0.09	7.84	±0.034	±21.5
20	0.500	2.25	6.76	0.16	0.06	7.84	6.76	±0.049	± 9.8
30	0.703	1.21	4.20	0.06	0.02	6.25	2.10	±0.037	± 5.3
40	0.787	0.64	2.72	0.02	0.01	3.42	0.81	±0.028	± 3.5
50	0.825	0.42	1.96	0.02	0.003	1.96	0.42	±0.022	± 2.7
60	0.844	0.30	1.69	0.01	0.003	1.32	0.25	±0.019	± 2.2
70	0.854	0.25	1.69	0.01	0.002	1.10	0.20	±0.018	± 2.1
80	0.858	0.20	1.82	0.01	0.002	0.90	0.16	±0.018	± 2.1

the overall uncertainties. However, these two elementary uncertainties are relatively small compared with other contributions and not included at present. An important observation from

Table 3.2 is that the uncertainty contributions from the terms (I), (II) and (VI) are generally more substantial than the contributions from (III), (IV) and (V) particularly at lower ethanol concentrations. This finding can be considered as a valuable guideline to design improvement of the *SPR* system to enhance its measurement accuracies.

A suggested improvement is to use 99.9% pure ethanol, a narrower band pass filter with 3-nm *FWHM* and a high precision mass scsale with a reading accuracy of 0.001g, i.e., $\omega_{\varepsilon_3} = \varepsilon_3 \times 0.000001 (\varepsilon_3 = n_3^2)$, $\omega_{\lambda_i} = 3\,nm$ and $\omega_c = 0.001g$. As a result, the uncertainty can be noticeably reduced for all ethanol concentrations, as shown in Fig. 3.7b; a particularly noticeable change occurs at 10% ethanol concentration, where the *SPR* reflectance uncertainty is substantially reduced to ± 8.2 % from the previous ± 21.5 %.

3.1.4 Summary

The technique of *SPR* reflectance detects the refractive index variations of the mixture with microscale spatial measurement resolutions and successfully measures the

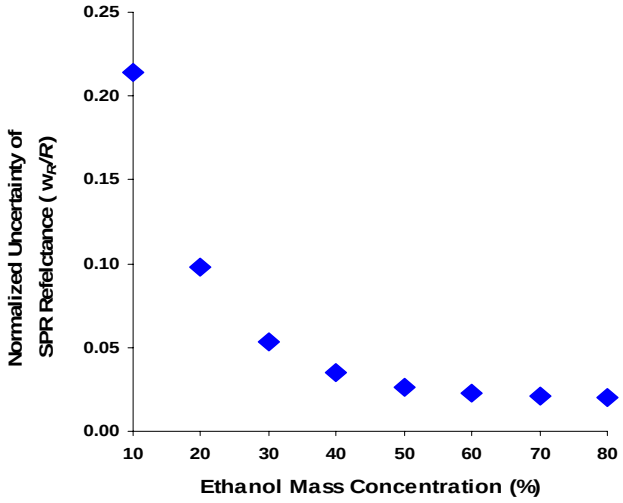

(a) 99.5% pure ethanol, 0.01g reading accuracy mass scale

$$\omega_{\varepsilon_2} = \pm 0.0438 + \pm i0.148\ (\varepsilon_2 = -13.2 + i1.25), \omega_{\varepsilon_3} = \varepsilon_3 \times 0.000025\ (\varepsilon_3 = n_3^2),$$
$$\omega_{\lambda_i} = 10\ nm, \omega_\theta = 1/60^o = 0.0167^o, \omega_{d_2} = 47.5\ nm \times 10\% = 4.75\ nm, \omega_c = 0.01g$$

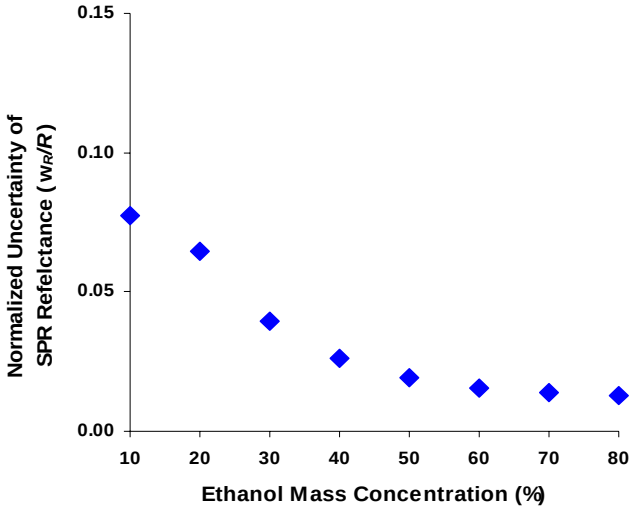

(b) 99.9 % pure ethanol, 0.001g reading accuracy mass scale

$$\omega_{\varepsilon_3} = \varepsilon_3 \times 0.000001\ (\varepsilon_3 = n_3^2), \omega_{\lambda_i} = 3\ nm, \omega_c = 0.001g$$

Figure 3.7 The normalized uncertainty for *SPR* reflectance (ω_R / R) as a function of ethanol concentration using nominal values of the related parameters ($\varepsilon_2 = -13.2 + i1.25$, λ = 632.8 nm, θ = 70.7°, and d_2 = 47.5 nm) and their elementary uncertainty levels: (a) for the present experimental conditions, and (b) for a suggested improved conditions [58].

time advancement of the mixing region of ethanol into water contained in a microchannel when the rapid penetration is driven by capillary phoresis. The spatial measurement resolution is estimated to 2.7 μm for the case of four (4)–pixel binning, while the limited lateral resolution is estimated to be less than 5.0 μm, based on the *SPR* wave attenuation length scale. The *SPR* visualization technique can be most effectively applied to various microscale fields, where introduction of foreign particles, such as tracking microspheres, fluorescence dyes or quantum dots, is detrimental in terms of biological compatibility, chemical and interfacial stability as well as physical consistency of fluid properties.

From the uncertainty analysis, several design guidelines are presented in order to refine the *SPR* imaging technique with higher measurement accuracies. The effect of concentration uncertainty of ethanol and water mixture (*c)* and ethanol purity (ε_3) on the overall uncertainty is generally higher than that of the dielectric constant of the gold layer (ε_2): thus, the use of a more accurate mass scale (reading accuracy better than 0.01g) and ethanol with extreme purity is recommended. For the case of wavelength uncertainty, or degree of monochromatically (λ), a laser light source with narrower bandwidth can theoretically increase the measurement accuracy; however, in reality it will obscure the *SPR* images with the diffraction rings, which appear extremely difficult to eliminate. Fine adjustment of the *SPR* angle (θ) is important to ensure the measurement accuracy, especially at lower concentrations, and the *SPR* angle should be carefully optimized to ensure minimum detectable *SPR* image intensity for the base fluid condition. The uncertainty due to the variation of metal film (Au) thickness seems to be most crucial (Table 3.2), except for the case of 10% or lower ethanol concentrations, and a custom-fabrication, whether using an e-beam evaporation, sputtering or electro-plating, is recommended to provide accurate control for the deposited metal layer. The last, certainly not the least important guideline, is that the related optical principle needs to be vigorously investigated to possibly alleviate the measurement limitation occurred from the reverse trend of refractive index at higher mixture concentrations.

3.2 Near-Wall Convective/Diffusive Saline Concentration Profiles

Historically, there have been various techniques developed for the measurement of salinity. Among these, three stand out for practical considerations: gravimetric, inductive electrical, and conductivity detection techniques. The gravimetric method is essentially the direct weighing of the specific gravity of a saline solution, however, this method has the shortcoming of a single-valued representation for a stationary situation. The induced electrical method is fast and considered to be acceptably precise and fast, but for high precision measurement of salinity, the conductivity measurement method is preferred because of its better measurement stability. The conductivity measurement technique, however, provides only point-wise detection at a time and features invasive electrode probes.

3.2.1 Experimental Methods and Calibration

In this part, *SPR* microscopic salinity detection tool is implemented and tested by measuring the time-dependent salinity distribution profiles in the near-wall region when a small saline drop (0.8 mm diameter) reaches the bottom of a water pool and spreads by convective-diffusion of salinity. The salinity distributions are determined from the measured *SPR* reflectance distributions using a calibration curve correlating with CCD gray level intensities. An elaborate uncertainty analysis identifies critical elementary uncertainties that needs to be improved to refine the measurement accuracies.

The experimental setup is based on the base of experimental system of section 3.1 (Fig. 3.1). The gold film layer is then illuminated by the *p*-polarized white light that is narrow-banded at 632.8 ± 1.5 nm using a 150W halogen bulb as white light source. The *SPR* reflectance images are recorded with a 12-bit cooled CCD camera (Hamamatsu Inc, Model C8800-21C).

The CCD pixel gray levels are correlated with specified saline concentrations to provide a calibration for salinity measurements. The saline concentration (C) is a function of the pixel gray level (*PGL*) recorded for *SPR* reflectance (R) as:

$$C = f(R \propto PGL) \qquad (3.4)$$

where f represents a functional form of complicated Fresnel's equation [6,34, 51,58,60,69-71].

Figure 3.8a shows *SPR* reflectance characteristic curves, calculated using the Fresnel's equation, at four different saline mass concentrations as functions of the incident angle. The minimum reflectance on each curve occurs at the so-called *SPR* angle specified for the corresponding saline concentration, and the *SPR* angle progressively increases from 70.7° at pure water to 73.0° at 10% NaCl mass concentration. The intersections of the vertical dashed line, drawn from the *SPR* angle of 73.0° for 10% salinity, indicate the *SPR* reflectance values at the four concentrations corresponding to the four curves.

The solid curve in Fig. 3.8b shows the approximately linear correlation between the measured pixel gray levels and the calculated *SPR* reflectance for the tested salinity range up to 10%. The error bars indicate the 95% uncertainty intervals for the pixel-to-pixel variations. Based on this linearity, the normalized *SPR* reflectance R is defined as

$$R = \frac{PGL - PGL_L}{PGL_H - PGL_L}(R_H - R_L) + R_L \qquad (3.5)$$

where the subscripts H and L refer to the maximum (10%) and minimum (0%) saline concentrations, respectively, and R_H and R_L are corresponding *SPR* reflectance intensities that are calculated using the Fresnel's equation. With two known pixel gray levels PGL_H and PGL_L, R at any unknown saline concentration at each pixel is evaluated from Eq. (3.5) as a function of PGL. The resulting saline concentration is determined from the Fresnel's equation, Eq. (2.2~2.6,3.4). The solid curve in Fig. 3.8c shows theoretical values calculated from Fresnel's equation and normalized pixel gray levels are directly related with *SPR* reflectance by Eq. (3.5) for the range of salinity from 0 to 10%. The symbols represent measured normalized pixel gray levels and show fairly good agreement, with the predictions with an average rms deviation of 0.062. The error bars represent the 95% confidence interval for the measured data assuming Gaussian distributions. The calibration curve shown in Fig. 3.8b is used to convert the measured

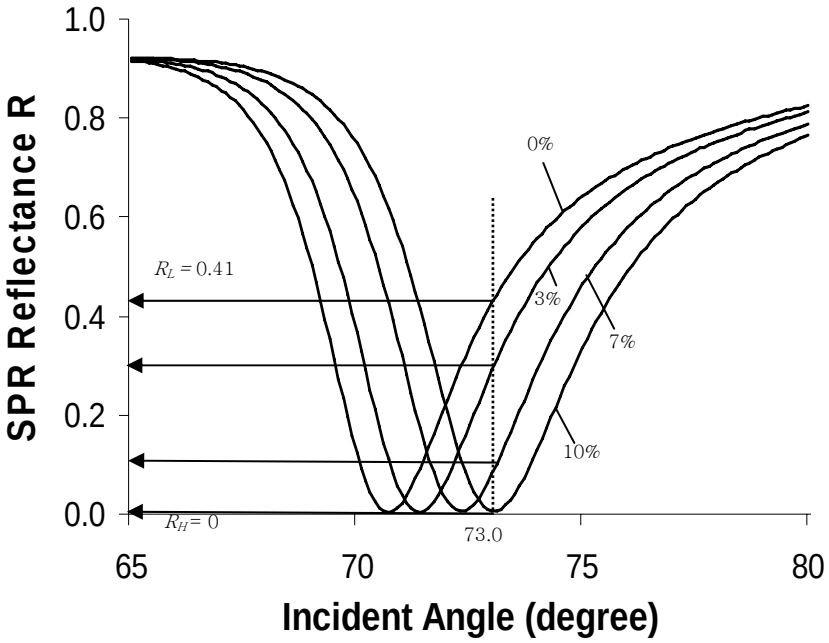

(a) *SPR* reflectance as functions of optimized *SPR* angles corresponding to salinity

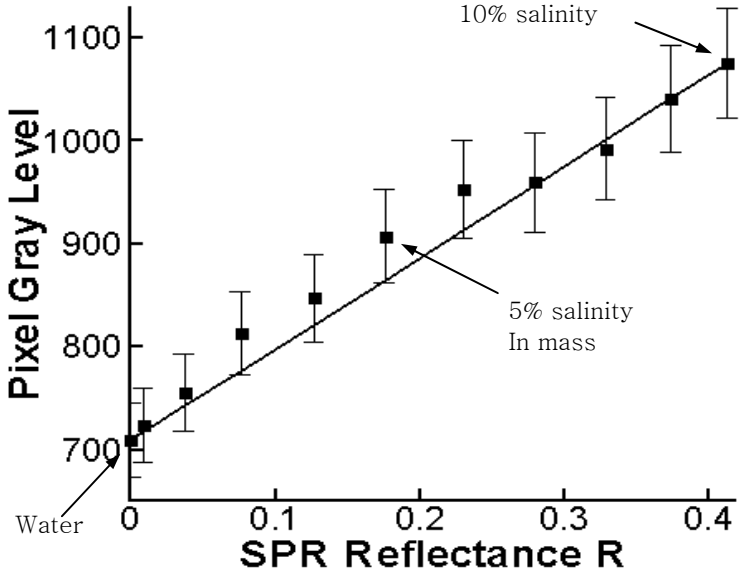

(b) A linear correlation between the measured pixel gray levels and the calculated *SPR* reflectance

Figure 3.8a, b, c *SPR* reflectance and calibration for salinity [60,69].

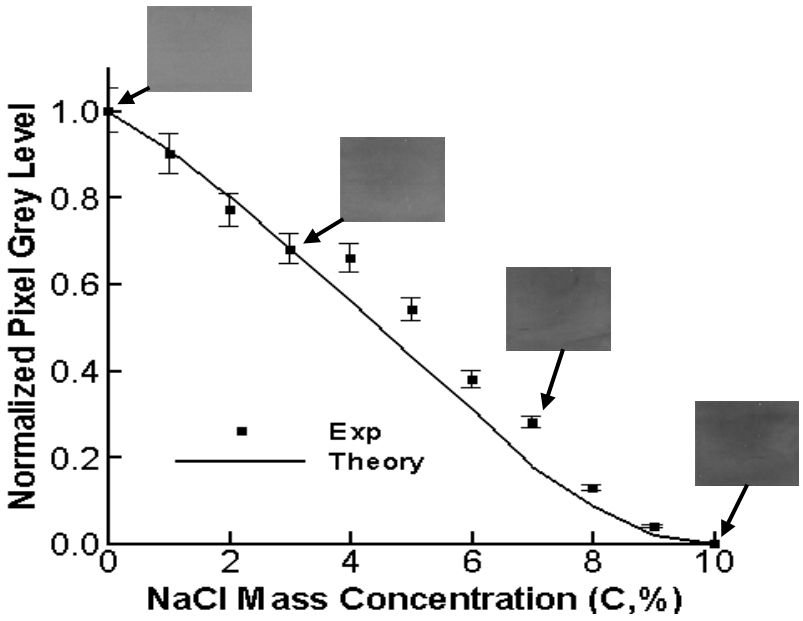

(c) Experimental calibration results for the normalized pixel gray levels

pixel gray levels into corresponding saline concentrations. Inset photos show actual *SPR* reflectance images taken at the four specified saline concentrations.

3.2.2 Results and Discussion

Figure 3.9 presents the dynamic and full-field detection of near-wall salinity when a 0.8-mm diameter aqueous drop containing 10% saline mass falls in a water bath (water depth of approximately 3mm). The saline drop (SG = 1.02) falls by gravity toward the bottom surface of gold metal layer and goes through convective (driven by gravity and inertia)-diffusive (driven by viscous and concentration gradients) process into the surrounding water. The first column shows the original *SPR* reflectance images of temporally developing salinity profiles at the near-wall region, with the *SPR* angle of 73.0° optimized for 10% salinity (i.e., 10% salinity corresponds to the lowest *PGL*). The second column presents corresponding full-field salinity distributions based on the calibration curve in Fig. 3.8c, and the third column represents the centerline salinity profiles. The fourth column schematically illustrates the development of the falling saline drop, showing its satellite droplets, and their settling evolution on the surface by convective-diffusion under the gravity field.

The evolution/diffusion of salinity is further described: (a) multiple satellite droplets are almost always generated at the result of the complicated vorticity interactions of a falling drop with the surrounding fluid, multiple satellite droplets are generated almost always, (b) the first satellite droplet of high salinity reaches the bottom surface resulting in the local salinity near the center to increases, (c) when the second satellite droplet reaches the bottom surface and joins the first droplet under diffusing, the resulting salinity further increases in the center region, (d) the main drop is then developed into a “donut” ring shape because of the balance between the viscosity and the interfacial tension with the surrounding fluid, and it reaches the bottom surface resulting in a concentric salinity distribution, (e) the convective-diffusion of salinity spreads out the concentric ring, while the additional falling of the main saline drop slightly increases the salinity in the concentric region, (f) the diffusion-dominated stage is reached eventually, and finally, (g) the localized salinity diffuses nearly entirely to zero salinity after a

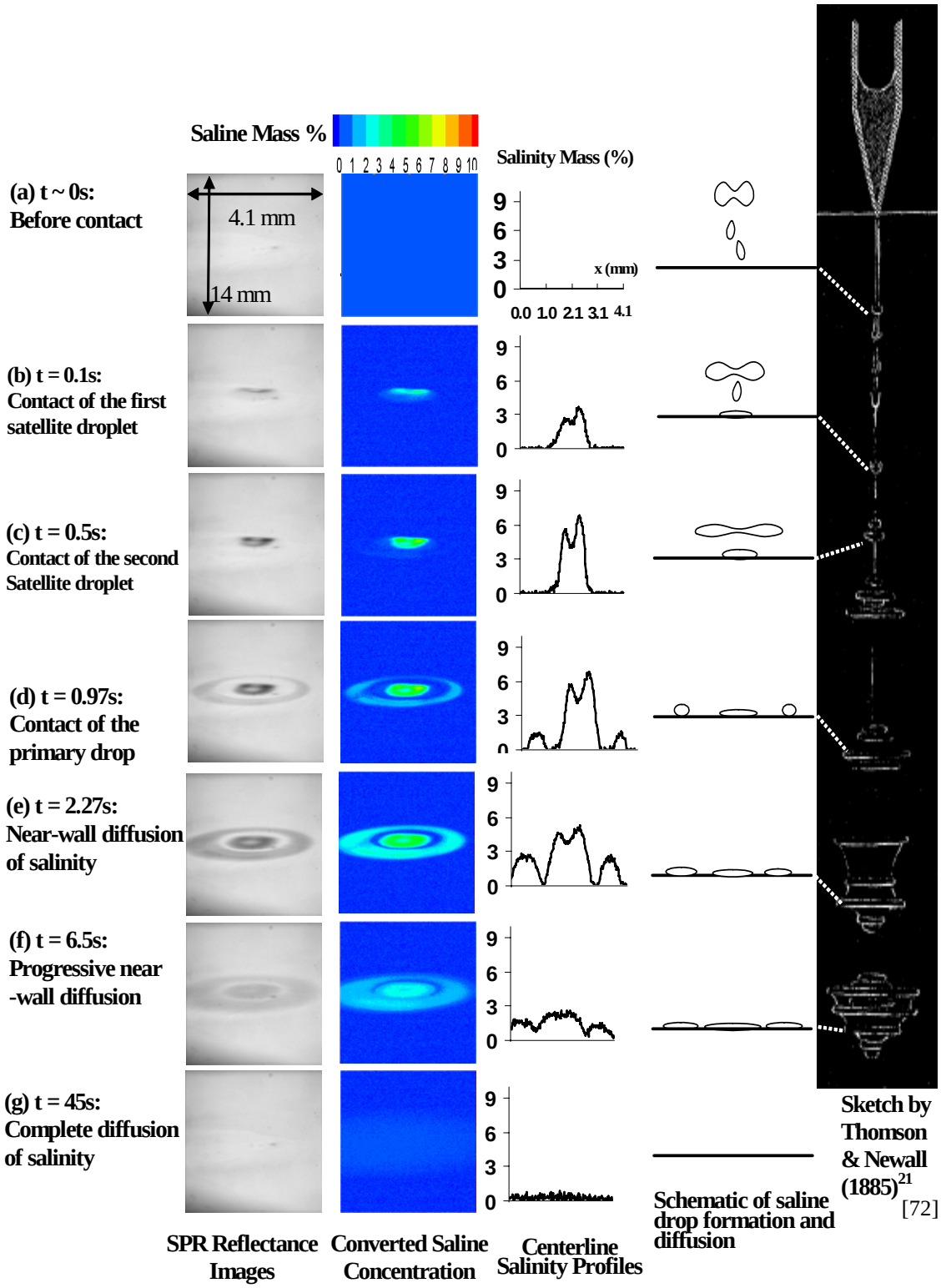

Figure 3.9 Full-field and real-time mapping of near wall salinity when a 0.8-mm diameter drop with 10% saline mass concentration is dropped into 3-mm thick pure water.

The first column shows the original *SPR* images, the second column shows the corresponding saline mass concentration fields based on the calibration curve presented in Fig. 3.8, the third column represents the centerline salinity profiles, the fourth column shows schematic illustrations of saline drop formation and near-wall diffusion characteristics, and the last column is the sketch made by Thomson and Newall [72] for the case of sulfuric acid (SG = 1.84, dynamic viscosity = 26.7cP) falling into water. The images shown in the first and second columns are vertically contracted by a factor of 3.42 because of the slanted viewing angle of θ_{SPR} = 73° from vertical for both incoming ray and *SPR* reflectance ray. Note that the apparently elliptic salinity profiles on the imaging domain are indeed circular ones in the physical domain [60,69,70].

considerable amount of time.

Note that the ring vortex occurs when the drop liquid is more viscous than the base liquid [73]. The viscosity of 10% NaCl aqueous solution is approximately 20% higher than that of pure water [61]. The interface between the NaCl aqueous solution and water is broadened because of the molecular diffusion progressively occurring during the convective-diffusion advancement. It is clear that the width of the ring becomes wider, and, accordingly, the saline concentration diffuses with increasing time.

According to Korteweg's theory, stresses due to gradients of concentration and/or density could conceivably give rise to the capillary phenomena, which are called capillary-like phenomena [73]. The evolvement of the saline drops on the gold surface demonstrates capillary-like phenomena for two miscible fluids of saline and pure water.

It is worthwhile noting that the capillary-like phenomena in two miscible fluids are not yet fully understood, and the *SPR* reflectance imaging system can experimentally delineate unknown physics of the capillary-like phenomena [69].

It is noted that the present results of Eulerian mapping of salinity taken at a fixed z-location show qualitative similarities with corresponding Lagrangian planes of the classic sketch of Thomson and Newall [72], as shown in the fifth column. Their sketch was based on their direct observation of a sulfuric acid (SG = 1.84, dynamic viscosity = 26.7cP) drop falling into water.

Uncertainty Analysis

The uncertainty analysis is conducted based on the single-point detection estimation given by Kline and McClintock (1953) [66]. The second-power equation referring to the measurement uncertainty of pixel gray level, which is proportional to the SPR reflectance *R*, is given as:

$$PGL \propto NPGL \propto R = R(\varepsilon_p, \varepsilon_t, \varepsilon_m, \theta, d_m, \lambda) \qquad (3.6)$$

$$\omega_R = \pm\left[\left(\frac{\partial R}{\partial \varepsilon_m}\omega_{\varepsilon_m}\right)^2 + \left(\frac{\partial R}{\partial \theta}\omega_\theta\right)^2 + \left(\frac{\partial R}{\partial d_m}\omega_{d_m}\right)^2 + \left(\frac{\partial R}{\partial \lambda}\omega_\lambda\right)^2\right]^{1/2} \qquad (3.7)$$

where ε_p, ε_t, and ε_m are dielectric constants of the prism (BK-7), tested saline solution, and the thin Au layer, respectively. θ is the incident SPR angle optimized for 10% salinity (73.0°), d_m is the thickness of the Au layer (47.5 nm), and λ is the incident wavelength (632.8 nm). The elementary uncertainty for the variation of the dielectric constant of the BK-7 prism, ε_p, is assumed negligibly small, 10^{-4} or 0.01%. The elementary uncertainty of the tested saline solution is also regarded as negligible. The other elementary uncertainties are best estimated as, :

$$\begin{aligned} &\omega_{\varepsilon_m} = \pm 0.0438 + \pm i 0.148\ (\varepsilon_m = -13.2 + i1.25)^{23},\ \omega_\theta = \pm 1/60^o = \pm 0.0167^o, \\ &\omega_{d_m} = 47.5\ nm \times \pm 2.5\%\ (= \pm 1.188\ nm),\ \omega_\lambda = \pm 1.5\ nm \end{aligned} \qquad (3.8)$$

The individual derivatives of *R* directly using Eq. (3.7) are too complicated to derive in their closed forms, primarily because of the nonlinear coupling with complex refractive index of gold. Alternatively, numerical estimations for the derivatives have been conducted using the first-order finite differential scheme as follows:

$$\omega_R = \pm\left[\left(\frac{\Delta R}{\Delta \varepsilon_m}\omega_{\varepsilon_m}\right)^2 + \left(\frac{\Delta R}{\Delta \theta}\omega_\theta\right)^2 + \left(\frac{\Delta R}{\Delta d_m}\omega_{d_m}\right)^2 + \left(\frac{\Delta R}{\Delta \lambda}\omega_\lambda\right)^2\right]^{1/2} \qquad (3.9)$$

: : : :

(I) (II) (III) (IV)

where each term represents an elementary uncertainty for SPR reflectance associated with the dielectric constant of gold thin film (I), the incident angle (II), the Au film thickness (III), and the incident light wavelength (IV). The effect due to the variation of the wavelength (IV) is negligible compared with the other three terms.

The differential ΔR in each elementary term is calculated for the range equivalent to the corresponding elementary uncertainty magnitude with respect to the specified test condition parameter. For example, for the case of term (IV), $\Delta\lambda == [\lambda + \omega_\lambda] - [\lambda - \omega_\lambda] = 2\omega_\lambda$ and $\Delta R = R(\lambda + \omega_\lambda; \varepsilon_m, \theta_{SPR}, d_m) - R(\lambda - \omega_\lambda; \varepsilon_m, \theta_{SPR}, d_m)$, where the elementary uncertainty is given as ω_λ = ±1.5 nm. Note that all other parameters are taken as their test condition values, i.e., $\varepsilon_m = -13.2 + i1.25$, θ_{SPR} = 73.0°, and d_m = 47.5nm.

Table 3.3 shows the summary results of uncertainty calculations, including magnitudes of the individual terms contributing in Eq. (3.9) for the range of NaCl aqueous solution concentrations from 0 to 8%. The overall uncertainty of *R* is as high as ±0.011 at 0% concentration, which is equivalent to ±2.7% in reflectance. Results show a dramatic decrease of overall uncertainty to ±0.002, or equivalent to ±4.1% in reflectance, at 8% salinity mass concentration. An important observation from Table 3.3 is that the uncertainty contributions from the terms (I) and (III) are generally more substantial than the contributions from (II). Therefore, it is observed that the dielectric constant and the thickness of the metal (Au) film are the two most significant factors in determining the

Table 3.3 Measurement uncertainties for *SPR* reflectance *R* and its three individual contributions ($\varepsilon_m = -13.2 + i1.25$, λ = 632.8 nm, θ_{SPR} = 73.0° and d_m = 47.5 nm)

NaCl Concentration (Mass %)	Reflectance R	Individual uncertainty terms in Eq. (3.9) ($\times 10^4$)			Overall Uncertainty ω_R
		I	*II*	*III*	
0	0.414	0.90	0.02	0.36	±0.011
2	0.330	0.56	0.02	0.25	±0.009
4	0.231	0.16	0.03	0.09	±0.005
6	0.127	0.00	0.03	0.01	±0.002
8	0.038	0.00	0.01	0.01	±0.002

overall measurement uncertainties for SPR reflectance.

3.2.3 Summary

SPR reflectance microscopy is devised to quantitatively measure salinity field distributions in the near-wall region where the *SPR* is effective. The successfully tested label-free, full-field and real-time mapping technique overcomes the limitation of single-point detection of practically all existing salinity detection techniques. The salinity-calibrated *SPR* microscopy system allows for the detailed and dynamic mapping of the near-wall salinity distributions with a lateral spatial resolution of about 4 μm when a gravity-falling 10% saline drop reaches the bottom of a shallow water pool. From the Kline-McClintock uncertainty analysis, the elementary uncertainties due to the variation of metal (Au) film's dielectric constant and its thickness seems to be most crucial in determining the overall measurement uncertainties.

3.3 Full-Field and Real-Time *SPR* Imaging Thermometry

Despite the known best sensitivity of *SPR* to the refractive index of the contacting medium (as fine as 10^{-8} RIU [48]), the *SPR* thermometry technique utilizing the RI-*T* correlation has not been well exploited to date. Limited *SPR* thermometry tests have been conducted to examine a single-point temperature detection of thin metal films [22,26,27,53], and very few *SPR* tests have been done for the case of liquid contacting medium [58-60]. None of these results, however, supplies temperature measurements in a full-field and real-time manner. Note that neither incident-angle scans [22,23] nor incident-wave spectral scans [27,28] can provide a "real-time" detection of transient test fields. At present, *SPR* imaging at a fixed angle is devised to allow real-time recording of transient thermal phenomena.

The two primary optical parameters, the refractive index of the prism and the refractive index of the thin gold film coated on the prism, are examined using the Fresnel theory [34] to determine their effects on the temperature dependence of *SPR* reflectance intensity. Based on the examinations, the most desirable selection of design parameters is proposed for improved measurement sensitivities for *SPR* thermometry. Furthermore, the

feasibility of real-time and full-field *SPR* thermometry is tested for two cases of time-varying temperature fields when a hot water droplet diffuses on the gold surface in either an air or water environment.

3.3.1 Experimental Methods

The *SPR* reflectance *R,* for a three-layer configuration (Fig. 3.10a) with the prism (1), the thin metal film (2), and a test medium (3), is given as a function of temperature:

$$R(T) = R[n_1(T), n_2(T), n_3(T), d_2, \lambda_I, \theta] \qquad (3.9)$$

where n is the refractive index, d_2 is the Au film thickness, λ_I is the incident ray wavelength, and θ is the incident ray angle. For the case of fixed d_2 (= 47.5 nm) and λ_I (= 632.8 nm), R varies exclusively with the refractive indices of n_1, n_2, and n_3.

The refractive index of the prism, n_1, is specified by the prism material, and its temperature dependence is assumed to be negligibly small [27]. The refractive index of a thin metal film, n_2, is given by the Drude model [52] as:

$$n_2(T) = n_r + in_i = \sqrt{\varepsilon_2} = \sqrt{1 - \frac{\omega_p^2}{\omega(\omega + i\omega_c)}} \qquad (3.10)$$

where ω is the angular frequency of the incident wave field, and $\omega_p(T)$ and $\omega_c(T)$ are the plasmon frequency and the collision frequency of the thin metal film material, respectively [26,27]. The plasmon frequency $\omega_p(T)$ is given as:

$$\omega_p = \omega_{p0}[1 + 3\gamma(T - T_0)]^{-1/2} \qquad (3.10a)$$

where ω_{p0} is the plasma frequency at reference temperature T_0, and γ is the thermal linear expansion coefficient of thin metal film. The collision frequency is determined as followings:

$$\omega_c = \omega_{cp} + \omega_{ce} \qquad (3.10b)$$

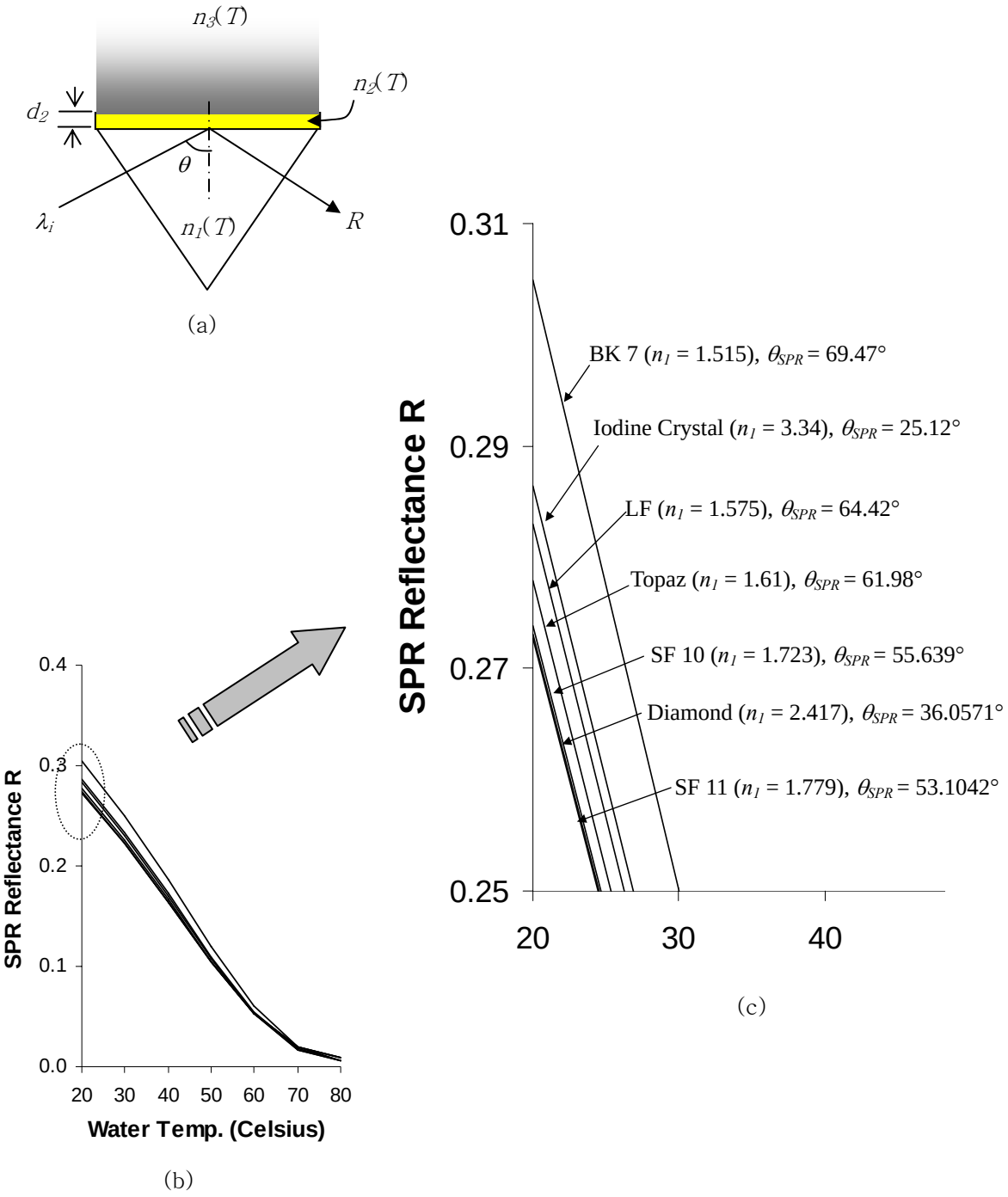

Figure 3.10 *SPR* reflectance *R* as functions of water temperature seven (7) different prism materials using the dielectric constant of Kolomenskii [54] for a thin Au film of 47.5 nm thickness [71].

where the photon-electron scattering frequency is defined as $\omega_{cp}(T) = \omega_0[\frac{2}{5} + 4(\frac{T}{T_D})^5]\int_0^{T_D/T} \frac{z^4}{e^z - 1}dz$, and the electron-electron scattering frequency is given as $\omega_{ce}(T) = \frac{1}{6}\pi^4 \frac{\Gamma\Delta}{hE_F}[(k_B T)^2 + (\frac{h\omega}{4\pi^2})^2]$. Parametric values used for calculations throughout are from Table 2.1.

Note that both temperature-dependent frequencies ω_p and ω_c alter the resulting *SPR* reflectance *R*. The temperature dependence of the test medium $n_3(T)$ of water is provided from the CRC Handbook [61].

3.3.2 Results and Discussion

Figures 3.10b and 1c show the temperature dependence of *SPR* reflectance for the seven different tested prism materials using water as the test medium. The *SPR* optimum angle is set for water at 80°C. While $n_2(T)$ is theoretically expressed in a closed form in Eq. (3.10,3.10a,b), the plasma frequency ω_{p0} needs to be experimentally determined using at least one refractive index value measured at a specified temperature in order to complete the calculations. The Kolomenskii's data [54] are selected to calculate ω_{p0} and determine $n_2(T)$, and successively $R(T)$ from Eq. (3.9).

The BK 7 prism shows the steepest gradients and the highest *SPR* reflectance intensity whereas the SF 11 prism shows the lowest *SPR* reflectance intensity. As the refractive index of the prism, n_1, increases, *R* decreases consistently. On the other hand, the optimum *SPR* angle persistently decreases with increasing n_1. Among the seven materials tested, the BK 7 prism seems to show the highest sensitivity for the temperature dependence of *SPR* reflectance when water is the test medium.

Figure 3.11a shows the *R-T* correlations for seven different sets of published refractive index data for thin Au films with thicknesses ranging from 45 to 48 nm (except for Palik's [74] case for 10 ~ 25-nm thicknesses), and Fig. 3.11b shows the corresponding normalized *R-T* correlations. The aforementioned BK 7 prism is used and the temperature dependence of the Au film's refractive index, $n_2(T)$ or $\varepsilon_2(T)$, is accounted for as in the case of Fig. 3.10. The seven measured refractive index values [13,14,21,54]

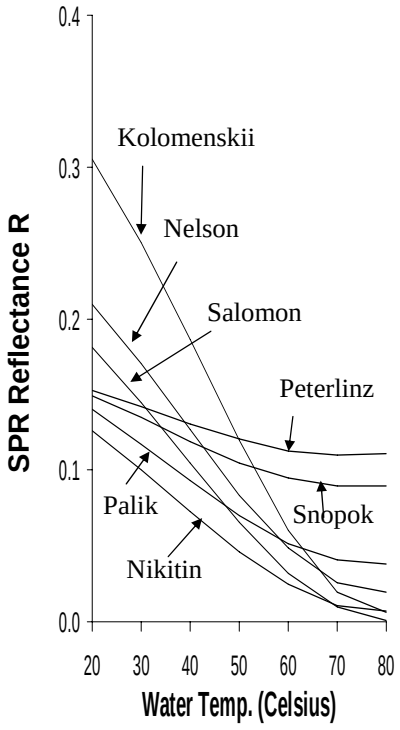

(a)

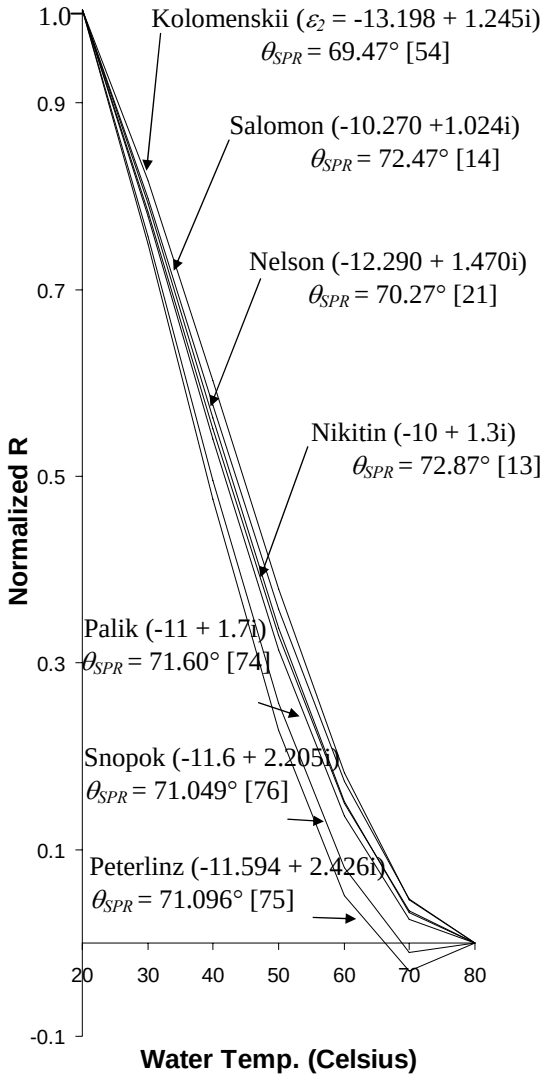

(b)

Figure 3.11 *SPR* reflectance *R* as functions of water temperature for seven (7) different refractive index values measured for thin metal films of approximately 47.5 nm thickness, coated on the top surface of a BK 7 prism (n_2 = 1.515) [71].

for thin Au films of approximately the same thickness show deviations between them that may be attributed to different measurement techniques and the preparation of the specimens, such as differences in surface roughness, dimensional uncertainties, and differences in fabrication processes. The largest deviation of ε_{2r} is approximately 15% (Kolomenskii [54]) over the average while the largest deviation of ε_{2i} is up to 50% (Peterlinz [75]) above the average. On the other hand, the *SPR* optimum angle θ_{SPR} shows a mere ±2.5% deviation, and this can be partially attributed to the dominating dependence of θ_{SPR} on ε_{2r}, with its relatively narrower deviation range, compared with ε_{2i}. The optimum *SPR* angle is given as $\theta_{spr} = \sin^{-1}\left[\frac{1}{n_p}\left(\frac{\varepsilon_m \varepsilon_s}{\varepsilon_m + \varepsilon_s}\right)^{1/2}\right]$ from the Kretschmann theory [34]. So. the *SPR* optimum angle cahnge can be approximately expressed as $\Delta\theta_{spr} \cong -\frac{\varepsilon_3^{3/2}}{2n_1\varepsilon_{2R}} > 0$. The *R-T* correlation gradient, $\Delta R/\Delta T$, represents the sensitivity of the *SPR* reflectance change corresponding to a unit temperature change; thus, the steepest gradient shown for Kolomenskii data (Fig. 3.11a) is expected to provide the highest measurement sensitivity. Both Peterlinz' [75] and Snopok's [76] data are considered inappropriate because of the deflections occurring for $T > 60$°C (more clearly visible in Fig. 3.11b). The possibly overestimated values of ε_{2i} for these two cases are believed to cause the undesirable deflections. The normalized *R-T* correlations of the remaining five cases collapse into a nearly single curve despite the noticeable discrepancies in their ε_{2r} as well as their ε_{2i}.

The experimental set-up for full-field and real-time *SPR* reflectance imaging thermometry (Fig. 3.12a) is designed and fabricated based after Kretschmann's configuration [34]. The system uses a BK 7 prism with 47.5-nm thick Au film coated on its top surface. Example results of *SPR* thermometry measurements are presented for dynamic temperature field developments when a hot water droplet at 80°C contacts the Au film surface at 20°C and spreads either in an air environment (Fig. 3.12b) or a water environment (Fig. 3.12c). The most favored *R-T* correlation, based on the Kolomanskii's n_2, is used to convert the recorded *SPR* image intensity distributions into corresponding

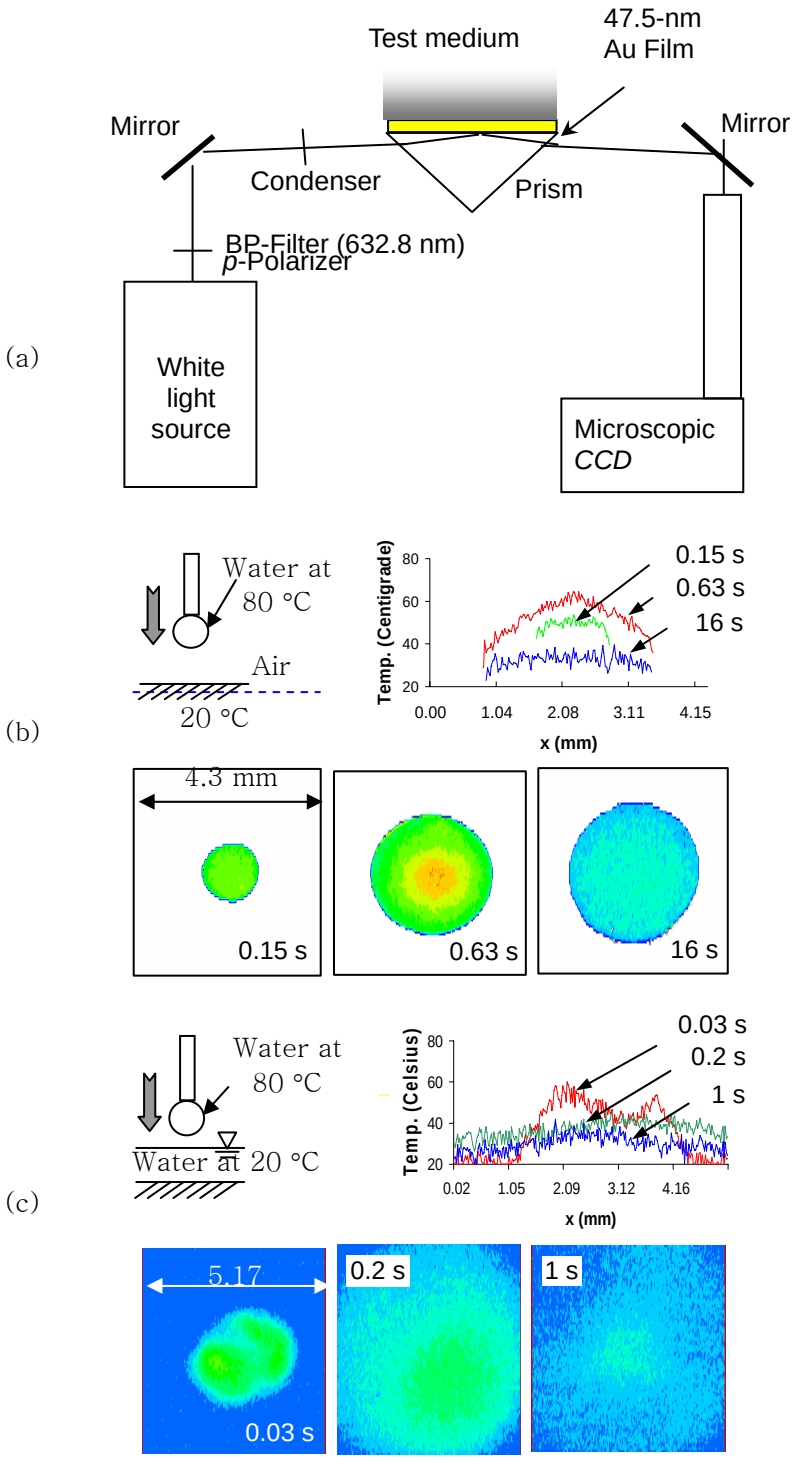

Figure 3.12 Full-field and real-time mapping (a) of transient temperature fields when a hot water droplet (80°C) falls on the cold Au surface (20°C) in (b) air environment and (c) water environment [71].

temperature fields. The gradual heat and energy transport under the air environment allows the contact surface shape to remain circular and spread concentrically, and the surface temperature gradually decreases to the environmental level after 16 seconds. In the cold-water environment, however, the aggressive single-phase mass and energy diffusion of hot water deforms the contact surface shape and spread, and the contact surface temperature rapidly approaches the environmental level in the relatively short time period of 1 second.

The temporal resolution of *SPR* thermometry depends exclusively on the data acquisition rate of the *CCD* camera recording system (6.4 ms or 156 fps for the present condition), while the spatial resolution is known to be specified equivalent to the propagation length of surface plasmon wave, which is a function of the incident ray's wavelength, the dielectric constant of the thin metal film, and the dielectric constant of the test medium [44]. For the present experiment, the theoretically minimum spatial resolution is estimated to be approximately 4.5 μm.

Using the Kline-McClintock analysis [66], the elementary uncertainties are calculated as followings:

$\omega_{d_m} = 47.5\,nm \times \pm 1.25\%\ (= \pm 0.59375\,nm)$, $\omega_{\varepsilon_m} = \pm 0.002115 + \pm i0.081\ (\varepsilon_m = -13.2 + i1.25)$,

$\omega_\theta = \pm 1.0/60^o = \pm 0.0167^o$, $\omega_\lambda = \pm 1.5\,nm$, $\omega_T = \pm 0.1^O C$

where d_m is the thickness of the Au layer (47.5 nm), θ is the incident *SPR* angle optimized for the water temperature of 80 °C (69.47°), and λ is the incident wavelength (632.8 nm).

The overall measurement uncertainty of T is estimated to be ±1.85°C (3.3% in R) at 20°C and ±1.41°C (9.8% in R) at 70°C. The relatively large uncertainty levels are mainly attributed, firstly, to the excessive elementary uncertainties of the dielectric constant of the Au film, and secondly, to the fabrication uncertainties of the Au film thickness. The elementary uncertainty for the fluctuation of light intensity of highly DC regulated power supply is considered negligibly small.

3.3.3 Summary

The BK 7 prism together with the Au film dielectric constant of Kolomenskii suggests the most desirable sensitivity for full-field and real-time *SPR* imaging thermometry for water as a test medium. The present real-time *SPR* thermometry at a fixed *SPR* angle tends to increase the measurement uncertainties at the lower temperature range and its measurement accuracy critically depends upon the thickness and dielectric constant of the Au thin film. Therefore, to further enhance the measurement accuracies and uncertainties, it is strongly recommended that the dielectric constant of Au film be more accurately determined and that the film thickness be more precisely fabricated.

3.4 Correlation of Near-Field Refractive Index of Nanofluids with Surface Plasmon Resonance Reflectance

Nanofluid is a mixture of metallic nanoparticles (Au, CuO, Al_2O_3 etc.) with a base fluid (water, ethylene glycol etc.) and its thermo-fluidic properties is known to substantially alter with nanoparticle population [77,78]. In addition, the nanoparticle loadings result in higher effective refractive index (*ERI*) values than the base fluid [77,79,80] and the corresponding *SPR* reflectance intensity shows dramatic changes with nanoparticle concentrations [81]. Therefore, a quantitative correlation between *SPR* reflectance and nanofluidic ERI at different nanoparticle loadings will allow nonintrusive, dynamic and full-field determination of nanoparticle concentrations. Effective refractive index (*ERI*, n_{eff}) values for nanofluids containing 47 nm average Al_2O_3 nanoparticles are measured using the Abbey type critical-angle refractometry based on total internal reflection (*TIR*) [82,83]. The experiments are conducted at a constant humidity of 40 % and laboratory temperature of 21 ±0.5°C. Furthermore, *SPR* reflectance imaging is devised [58-60] and correlated with the *TIR* measurement to establish a real-time and full-field mapping of nanofluidic concentration fields.

3.4.1 Experimental Methods

Figure 3.13 shows measured *TIR* reflectance versus incident angle increase for

(a)

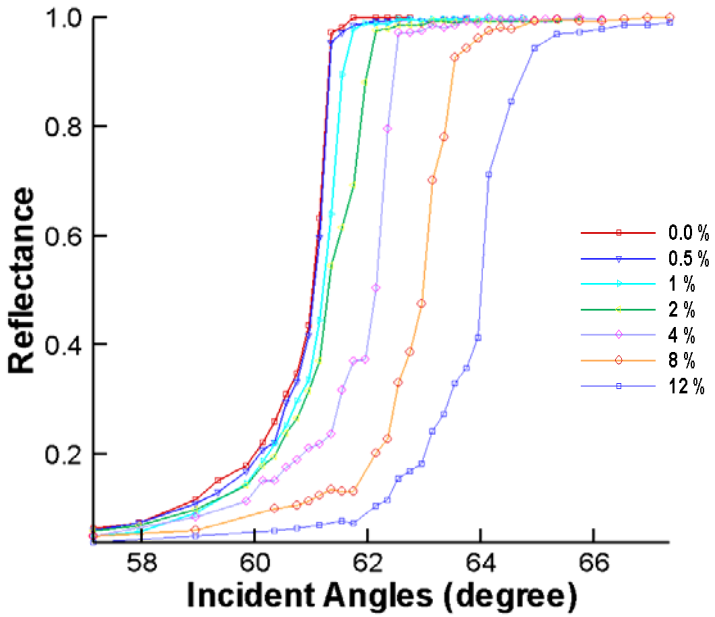

(b)

Volume concentration of nanoparticles (c, %)	Effective refractive index n_{eff}	Normalized uncertainty (ω_n/n_{eff}, %)
0	1.332	0.38
0.5	1.333	0.73
1	1.335	0.75
2	1.340	0.87
4	1.345	1.44
8	1.357	1.21
12	1.373	1.31

Figure 3.13 Experimental determination of effective refractive index (*ERI*) of nanofluids containing 47 nm Al_2O_3 nanoaprticles using total internal reflection (*TIR*) technique: (a) increasing reflectance with increasing incident angle, and (b) measured ERI and measurement uncertainties for different volume concentrations of nanoparticles [84].

the nanoparticle volume concentrations up to 12%. The 632.8 nm He-Ne laser light source is used with focused beam spot on the test sample with the diameter less than 0.5 mm to minimize the noise associated with the diverging beam effect. 3 μl volume of test sample is placed on top of BK7 prism (n_p = 1.515) and reflectance is measured by photometer (Newport Model 818 SL).

3.4.2 Results and Discussion

Snell's law ($n_{eff} = n_p \sin\theta_c$) calculates n_{eff} once the critical incident angle θ_c is identified. Since the critical point is broadened with increasing volume concentration, θ_c is determined at the turning point in the broadened range [79]. The measurement uncertainty associated with the critical angle broadening ($\Delta\theta$) is estimated using

$$\omega_n = \left(\frac{\partial n}{\partial \theta}\right)\Delta\theta = (n_p \cos\theta_c)\Delta\theta \qquad (3.11)$$

n_{eff} of nanofluids increases with increasing nanoparticle loadings and the normalized uncertainty (ω_n / n_{eff}) is shown to be less than 1.5% for the tested range of volume concentrations up to 12%.

A theory of real refractive index or effective RI, n_{eff} of non-interacting, spherical, colloidal particles for dilute dispersions is given [85];

$$n_{eff} = m_1 + \frac{3m_1 v}{8x} P'_{sca} \qquad (3.12)$$

where $x = 2\pi r m_1/\lambda$, r is radius of particle, v is volume fraction of nanoparticles, P'_{sca} is refraction efficiency as a function of $m = m_2/m_1$ with subscript 1 and 2 refer to the base fluid (m_1 = 1.332 for water at 20°C) and the nanoparticles (m_2 = 1.7 [86] for Al_2O_3), respectively. When the size of nanoparticle is much smaller than the wavelength ($d < \lambda/10$), Rayleigh scattering theory in the form by Van de Hulst [77,85,87] derives

$$P'_{sca} = 4x\left(\frac{m^2 - 1}{m^2 + 2}\right), \qquad m = m_2/m_1 \qquad (3.13)$$

Combining Eqs. (3.12) and (3.13) gives

$$n_{eff} = m_1 + \chi(m_2 - m_1)v\,, \quad \chi = \frac{3}{2}\left(\frac{m+1}{m^2+2}\right) \qquad (3.14)$$

If χ is exactly unity, $n_{eff} = m_1 + (m_2\text{-}m_1)v$, which is regarded as a volume average of refractive index values and also concurs with Mie scattering case as demonstrated for particles significantly larger than 100 nm [77]. For the present case of water and 47-nm Al_2O_3 particles, the Rayleigh theory gives $\chi = 0.94$, i.e.

$$n_{eff} = 1.332 + 0.345v \qquad \text{[Theory]} \qquad (3.14a)$$

whereas the present experiment extrapolates $\chi = 0.89$, i.e.,

$$n_{eff} = 1.332 + 0.327v \qquad \text{[Experiment]} \qquad (3.14b)$$

The discrepancy of approximately 5% is believed to be attributed to particle interactions of non-diluting nanofluids.

The three-layer configuration of *SPR* system (Fig. 3.14a) creates an evanescent wave field that is in a condition of total internal reflection when illuminated with *p*-polarized monochromatic light at λ. The top surface of the SF-10 prism is metal-deposited to lay a thin film and the free electrons in the gold film create a surface plasmon resonance when excited by the evanescent wave field at the optimum *SPR* angle. Fresnel theory is applied to calculate *SPR* reflectance *R* according to Kreschman' configuration [34] with the refractive index of prism $n_1 = 1.723$ (SF-10 prism), the dielectric constant $\varepsilon_2 = -13.198 + 1.245i$ for the gold film, thickness $d_2 = 47.5$ nm, $\lambda = 632.8$ nm, and the incident optimum angle of $\theta_{spr} = 56.3°$. Thus, *R* varies exclusively with the nanofluidic *ERI*, n_{eff}.

The correlation of normalized intensity *R* with the *TIR* measured n_{eff} (is presented for nanofluidic concentrations ranging from 0 to 12% in volume in Fig. 3.14b. The experimentally extrapolated correlation is given as (the dashed curve):

$$n_{eff} = 1.332\ exp(-0.000253R) + 7.854\times10^{-5}\ exp(6.093R) \qquad (3.15)$$

where *SPR* reflectance *R* is experimentally determined by averaging pixel gray levels recorded in each *SPR* image (inset photos) at a specified concentration.

The vertical error bar denotes the uncertainty analysis for *TIR* measurements as shown in the inset table in Fig. 3.13. The horizontal error bar represents the root-mean-

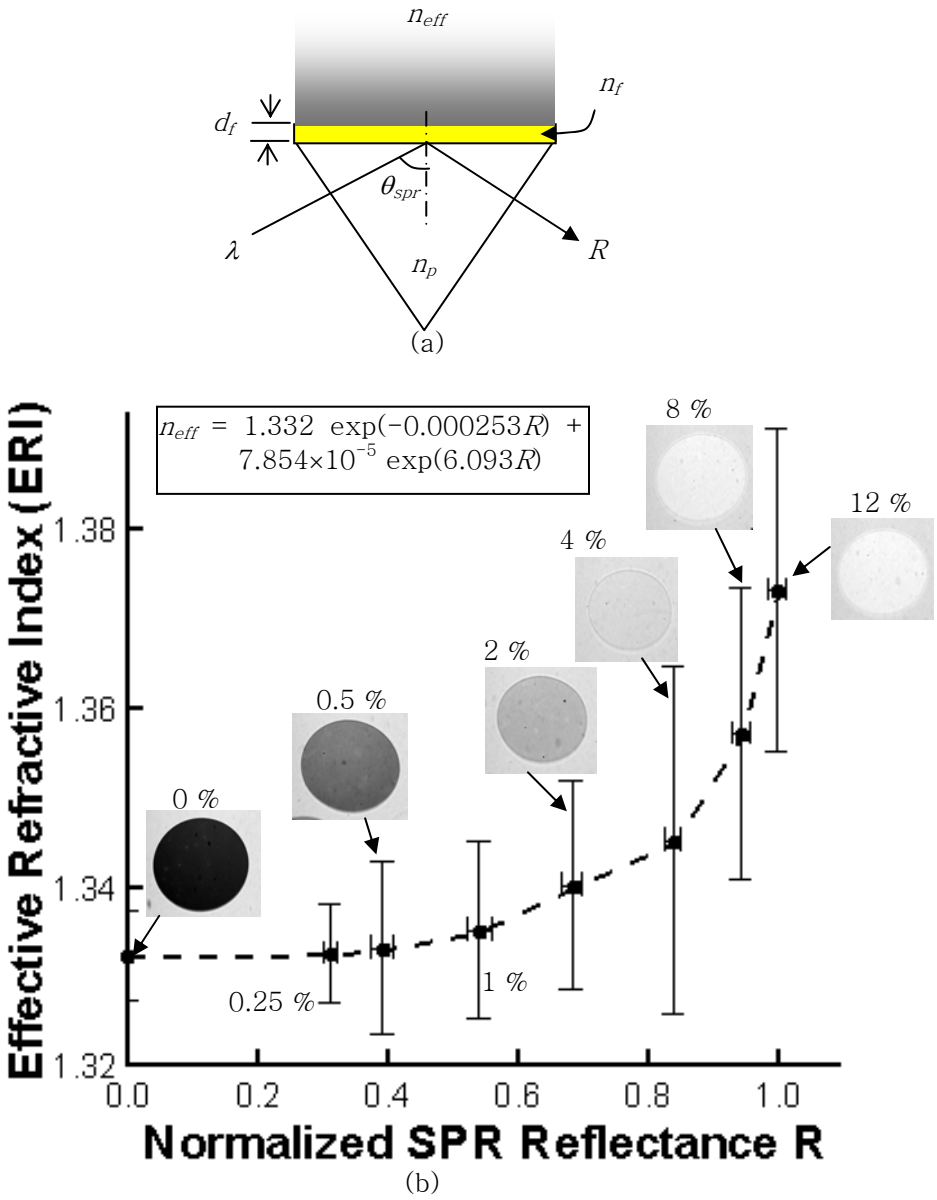

Figure 3.14 (a) a schematic illustration of *SPR* reflectance imaging, and (b) a correlation of *TIR*-measured ERI of nanofluids (47 nm Al_2O_3) with normalized *SPR* reflectance *R* for different loadings. The vertical error bars represent the measurement uncertainty of the *TIR* technique associated with the broadening of critical angles and the horizontal error bars represent the RMS of the spatial pixel intensity variations of *SPR* reflectance images [84].

square (RMS) variation of PGL in each image and this error is bounded within ±5%. *SPR* measurement uncertainties are estimated using the Kline-McClintock analysis [66] with the elementary uncertainties of $\omega_{d_m} = \pm 0.59375\, nm$, $\omega_{\varepsilon_m} = \pm 0.002115 + \pm i 0.081$, $\omega_{\theta_{spr}} = \pm 0.0167^o$, $\omega_\lambda = \pm 1.5\, nm$ [58]. The overall measurement uncertainty of *SPR* reflectance *R* is estimated to be less than ±7 % for all tested range. The uncertainties are mainly attributed to the elementary uncertainty of the dielectric constant of the Au film (ω_{ε_m}), and secondly, to the fabrication uncertainty of the Au film thickness (ω_{d_m}).

Use of both correlations of Eqs. (3.14b) and (3.15) allows experimental determination of near-field nanoparticle concentration fields that are continuously changing with time such as an evaporating drop of nanofluid (Fig. 3.15). An evaporating nanofluid drop of 1.0 μl containing 0.25% initial volume concentration of Al_2O_3 nanoparticles is placed on top of the gold thin film (the wet diameter of 1.6 mm) and allowed to slowly evaporate in the laboratory environment. The *SPR* angle of 56.3° is optimized for water so that *R* is the lowest for water. The *SPR* reflectance intensity (the first column) shows the darkest image at the lowest nanoparticle concentration at t = 0 and thereafter increases with increasing concentration as the evaporation is progressed.

The dominant evaporation in the edge draws nanoparticles and this phenomena is called “self-pinning” driven by the radially outward flow replenishing the evaporative flux near the edge [88]. The region of dense nanoparticles is created along the outer edge as shown by the bright ring in the *SPR* image at t = 283 s. The third and fourth columns present corresponding effective RI and volume concentration field distributions based on the ERI-*R*- concentration correlation as shown in Fig. 3.14. The outer ring region is measured to have ERI and volume concentrations higher than 12%.

As the evaporation further progresses, the outer region is solidified as self-assembly of nanoparticles (t = 326s) and the center fluidic region shrinks to be thinner and denser. Eventually the solidification penetrates inward into the thin film region (t = 327s) and complete dryout will be reached soon after that. Note that the ERI-*R*

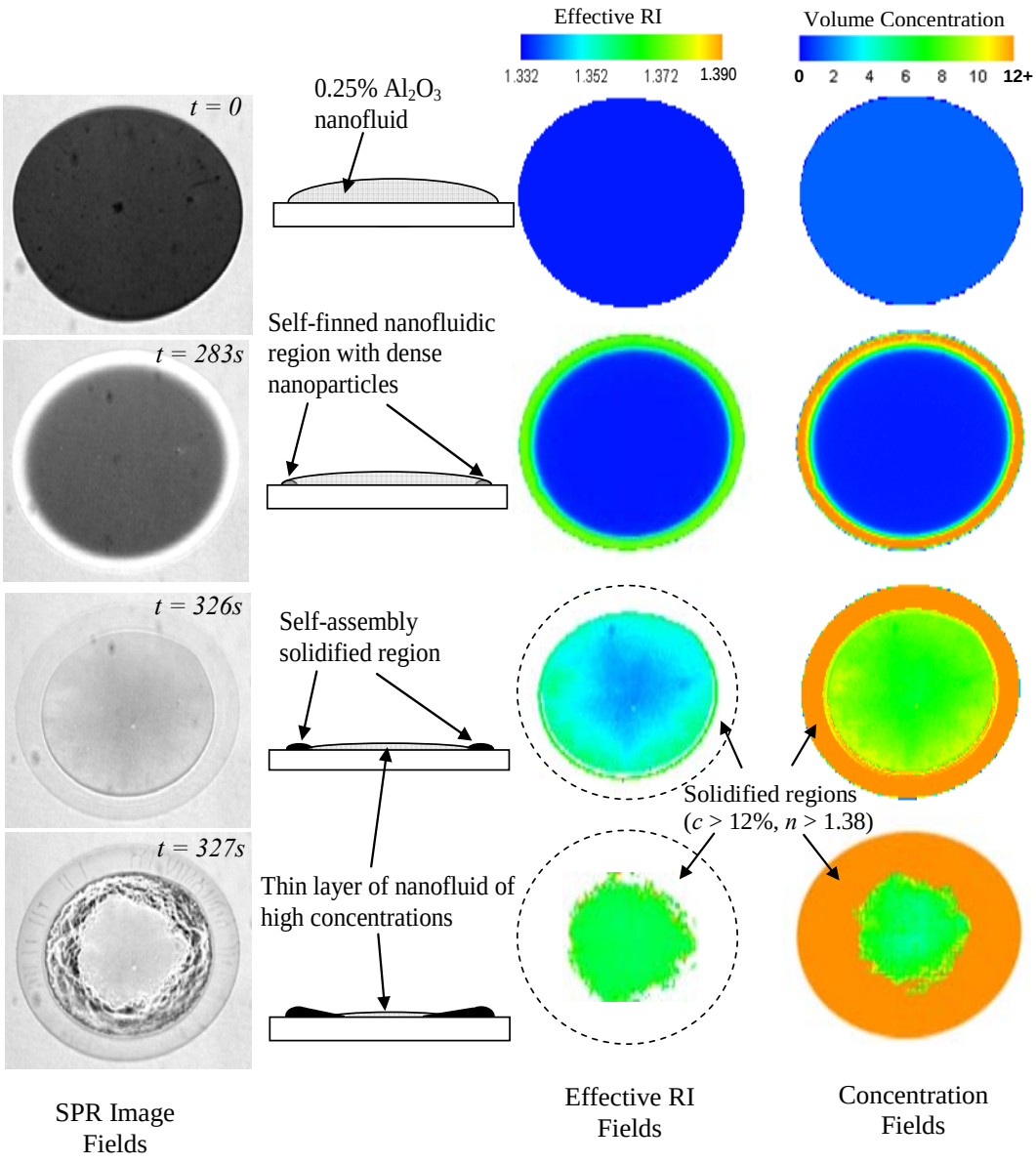

Figure 3.15 Full-field and real-time mapping of ERI and volume concentration distributions of evaporating nanofluid containing 47 nm Al_2O_3 nanoparticles. The tested nanofluid has an initial nanoparticle concentration of 0.25% in volume and is placed on top of Au thin film until the self-assembled dryout is reached. The first column shows progressive *SPR* reflectance images as the evaporation/self assembly is progressed, the second column presents schematic drawings illustrating the progress, the third column shows ERI field distributions based on the correlation of Fig. 3.14, and the fourth column shows corresponding concentration filed distributions [84].

correlation (Fig. 3.14) is valid only for fluidic regions of up to 12% volume concentration and cannot be applied once the solidification is initiated.

3.4.3 Summary

Nanofluidic ERI is determined by the Abby-type *TIR* and correlated with SPR reflectance image intensity. The resulting correlation enables determination of nano fluidic ERI and near-field concentration distributions in real-time and full-field.

Further, and significantly, the outcome of the research methodology allows us to quantitatively and dynamically examine the ERI distributions and nanoparticle concentration field evolution for evaporating nanofluid droplets containing 47 nm Al_2O_3.

3.5 Unveiling of Hidden Complex Cavities formed during Nanocrystalline Self-Assembly

How nanoparticle crystalline structures assemble themselves has been, to date, remaining as a largely unknown process at least for its dynamic and quantitative characterization. However, this process is attracting growing attention from researchers because of the important potential applications of these nanostructures, including nanoscale manufacturing and bioprocesses [88-93]. Since Deegan et al. [88] first delineated the ring stain formation, various attempts have been made to understand how crystallized patterns form from the evaporation-induced self-assembly of colloidal or nanoparticles.

Recently, possibility of a cavity structure was conjectured to accompany microtornadoes-like pattern of evaporating liquid during the evaporation-induced self-assembly process [94,95]. However, the existence of the conjectured hidden cavities has never been satisfactorily evidenced because of the difficulty associated with nonintrusively accessing the cavities, which are roofed by a thick nanocrytalline crust structure.

We are now able to demonstrate the existence of hidden hollow cavities by using *SPR* refractive index mapping [44,58-60,69-71] to fingerprint the near-field solid-gas phase distributions of the cavity structure, viewed from the bottom of the nanocrystaline

structure. Furthermore, we have been able to quantitatively reconstruct the fully three-dimensional cavity dimensions by digitally analyzing the naturally formed R-G-B interference fringes constructed by the reflected rays from the cavity inner walls.

3.5.1 Experimental Methods

The present crystallization experiments were conducted with an aqueous solution containing 10% volume of 47-nm average diameter Al_2O_3 nanoparticles (Fig. 3.16); the solution is laid on a gold surface at a constant humidity of 40% and a laboratory temperature of 21±0.5°C. No surfactant or additives were used in sonically mixing the 47-nm Al2O3 nanoparticles with deionized water at the authors' laboratory. Note that he 47-nm diameter is an average value for the inevitably distributed Al_2O_3 nanoparticles. It is expected that larger particles (than the average) will generally play more deterministic role in the formation of nanocrystalline structure than smaller particles because of their larger gravity and inertial effect. The effect of nanoparticle sizes on crystallization is definitely a critical issue to be more extensively and systematically examined in the future study.

The characteristics of evaporation-induced crystallization can vary with different types, sizes and concentrations of solutes, and also with the relative humidity of the atmosphere and the hydrophobicity and the morphology of the substrate [97-100]. Based on our observation, however, we believe that most cases of nanofluidic crystallization create one form or another of hidden cavity structures, which is attributable to the competing growth and decay of the solid-liquid-gas (s-l-g) phases during the self-assembled crystallization.

A combined optical recording system (Fig. 3.16) was implemented to simultaneously image both dorsal and ventral views of the nanocrystalline structure. Normal reflected optical microscopy is used for dorsal view imaging from the top. The *SPR* near-field fingerprinting [44,58-60,69-71] identifies the existence of hidden cavity structures viewed from the bottom, and the quantitative analysis of R-G-B natural fringes [96] delineates the complex inner dimensions of the 3-D cavity. Note that all three videos presented herein were recorded starting 10 minutes after the beginning of evaporation.

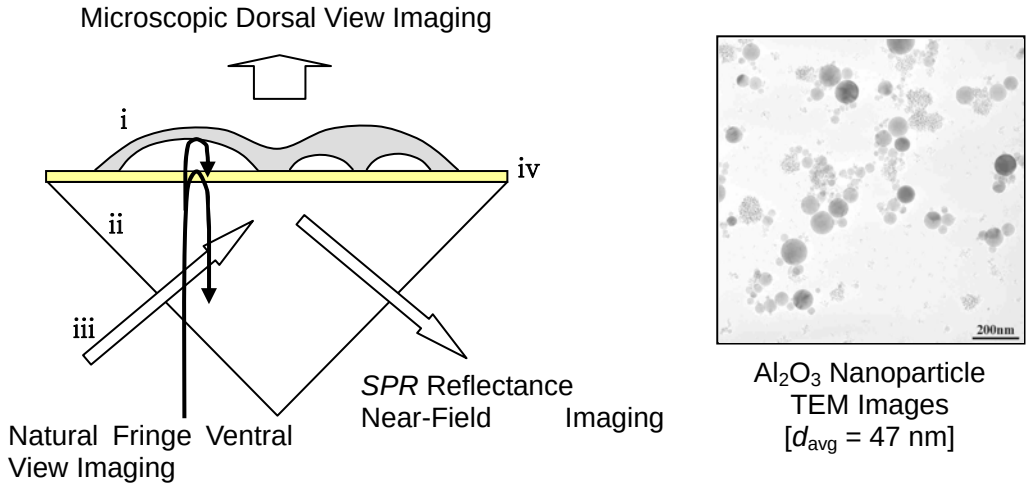

Figure 3.16 Simultaneous imaging of microscopic dorsal view from the top, near-field *SPR* fingerprinting, and natural fringe ventral view of the crystallized inner cavity structure (i). The SF-10 prism (ii) with n = 1.723 creates the evanescent wave field under total internal reflection conditions when illuminated with *p*-polarized monochromatic light at 632.8 nm (iii). The free electrons in the 47.5-nm thick Au thin film (iv), which is metal-deposited on the SF-10 prism, create surface plasmon resonance which is driven by the evanescent wave field and the resulting *SPR* reflectance distributes depending on the refractive index of the *s-l-g* phase distributions of the near-field cavity structure. Computer analysis of a full-field *R-B-G* natural fringe map allows quantitative reconstruction of the complex 3-D cavity details (see Fig. 3.18e) [81]**.**

The SF-10 prism (n = 1.723) creates an evanescent wave field that is in a condition of total internal reflection when illuminated with *p*-polarized monochromatic light at λ = 632.8 nm. The top surface of the SF-10 prism is metal-deposited to lay a thin gold film of 47.5 nm thickness and the free electrons in the gold film create a surface plasmon resonance when excited by the evanescent wave field. The resulting *SPR* reflectance distributes depending on the refractive index variations of the contacting test field and the resulting reflectance variations can distinguish the *s-l-g* phases of the near-field cavity structures.

3.5.2 Results and Discussion

An examination of dynamically recorded *SPR* images delineates the physical mechanism for the formation of hidden hollow cavities during the self-assembly of nanocrystalline structures. The *SPR* images shown in Fig. 3.17a map the evolution of near-field cavity structures by means of intensity discrimination among the phases; gas (gray), liquid (white) and solid (black) phases. The penetration depth of the *SPR* wave field is estimated to be 192 nm for the liquid phase and 353 nm for the gas phase, measured from the substrate gold surface. After a certain amount of time t from the beginning of evaporation, gas phase regions are conceived as cavity in the near-field. As the evaporation proceeds, the gas phase expands and the cavity structure grows while the liquid phase regions continually shrink (t +5s). The shrinkage stops when the nanoparticle concentration in the liquid phase exceeds a certain limit and the crystallization begins from the pinned edge region (t +10s).

Figure 3.17b shows a cross-sectional view normal to the dashed lines on the *SPR* images to provide a schematic picture of the 3-D self assembly mechanism. Anchoring of the nanoparticles starts soon after the droplet contacts the substrate surface; contact line is pinned with the radially outward flow (1) when evaporation begins [88,101]. The progressive evaporation lowers the surface temperature near the top dorsal area due to the latent heat loss, and consequently, a thermocapillary phoretic Marangoni flow (2) is induced toward the dorsal peak region having higher surface tension [92,101,102]. The “replenishing” flow (3) rises from the bottom to conform to a stagnant point [101,103]

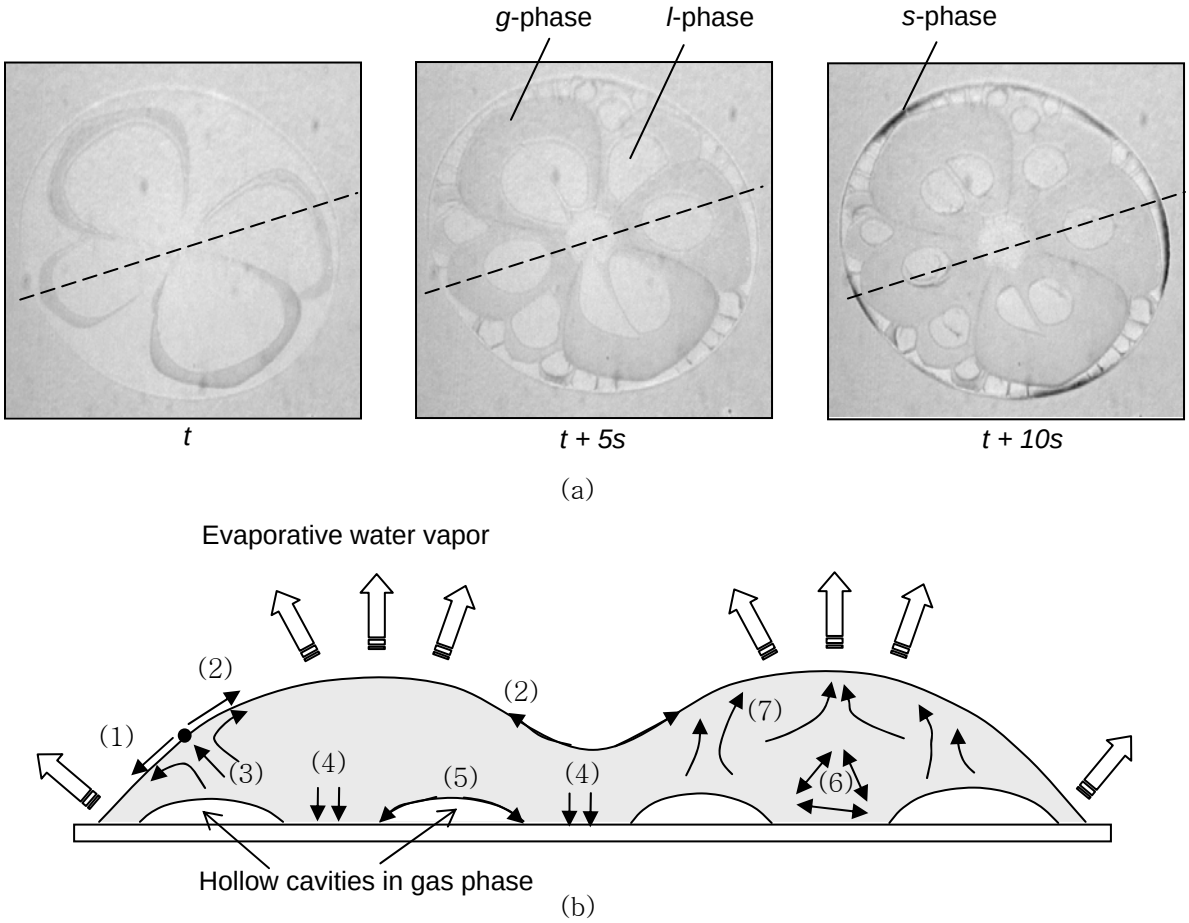

Figure 3.17 The *SPR* fingerprinting identifies the existence and layout of hidden cavity structures by distinguishing *s-l-g* phase regions. **(a)** Sequential *SPR* fingerprint images show the initiation of the gas-phase cavities (*t*); their growth, driven by the surface tension actions (*t* + 5s); and the progressive crystallization after the cavity growth has ceased (*t* + 10s). **(b)** The sketch schematically represents a cross-sectional view normally erected along the dashed lines on the *SPR* images showing the mechanism for the complex cavity formation; (1) self-pinning driven by the radially outward flow replenishing the evaporative flux near the edge, (2) Marangoni or thermocapillary phoretic flow driven toward the relatively cold top region, (3) stagnation flow generated by thermocapillary phoretic and replenishing flows, (4) internal anchoring driven by attractive interaction of nanoparticles with the substrate gold surface, (5) cavity growth driven by surface tension action, (6) attractive van-der-Waals force between nanoparticles, and (7) thermophoretic upward flow to replenish the evaporated liquid [81].

and ultimately draws vacuum in the near field to conceive a cavity. The downward forces (4) of the attractive van-der-Waals interaction of nanoparticles with the substrate surface result in multiple inside anchorings and conform to a complex hidden cavity structure.

The surface "tension" action associated with the cavity interface (5) continually expands the cavity areas with progressive evaporation until the nanoparticle concentration exceeds a fluidic limit and surface tension is no longer active. Aquatic evaporation also decreases the interparticular distance and increases the attractive van-der-Waals force (6), overcoming the electrostatic repulsive force between the slightly negatively charged Al_2O_3 nanoparticles [104]. This enhances the congregation of the nanoparticles and expedites the evaporation. The internally driven thermophoretic flow (7) along the temperature gradients from the ventral cavity ceiling to the dorsal peak area also contributes to further evaporation.

Rayleigh number which is a dimensionless number associated with free convection is estimated to be $Ra = Gr \cdot \Pr = g\beta\Delta T h^3 / \alpha\nu \approx 20$, where gravitational acceleration g = 9.81 m/s, thermal volumetric coefficient $\beta \approx 206 \times 10^{-6}$/K for 10% Al_2O_3 nanofluids [105], which is well below the critical value of 1,708 for the onset of natural convection inside the evaporating droplet. For calculation, the following parameters are assumed; maximum temperature differential between the dorsal and ventral surfaces $\Delta T \sim 1.4$K [106], droplet thickness $h \sim 1\ mm$, thermal diffusivity $\alpha \sim 145 \times 10^{-9}\ m^2/s$ taken for water, and kinematic viscosity $\nu \sim 0.961 \times 10^{-6}\ m^2/s$ for water.

The ratio of surface-tension-driven Marangoni flow to thermally driven convection flow [106] is estimated to be at approximately 60 for the present experimental conditions; using the approximations of $VM \approx B\Delta T/\eta$ and $VR \approx \beta\rho\Delta T g h^2/\eta$ [106], where surface tension variation with temperature $B \sim 1.5 \times 10^{-4}\ N/m$K for water, nanofluidic density $\rho = 1{,}258\ kg/m^3$, dynamic viscosity $\eta \sim 959 \times 10^{-6}\ Pa.s$ for water, the ratio of $VM/VR = B/\beta\rho g h^2 \approx 60$.

Thus, it can be said that the fine-scale nanocrystalline self-assembly process is dominated by conduction heat transfer, with minimal contribution from natural convection, strongly associated with the interfacial Marangoni flow, or so-called

thermocapillary phoresis.

Figure 3.18 shows the details of a self-assembled nanocrystalline structure and unveils the previously hidden complex cavities. The microscopic dorsal plane image is taken 2 minutes after the cavity inception (Fig. 3.18a) when the crystallization is completed. The crystallized glassy surface conforms to a half-toroidal shape with a number of radial crack lines [107,108]. The crystallized crust [99, 107-110] is approximately 2 mm in diameter and 160 μm in the maximum height.

The *SPR* image (Fig. 3.18b) shows two-dimensional fingerprint of the three-dimensional cavity structure. The dark image areas correspond to crystallized nanoparticles congregated on the aforementioned anchored regions, and the bright background represents the air interface, both inside and outside the crust. Each anchored spot is located in the middle of the corresponding compartment, which is divided by the primary crack lines shown in Fig. 3.18a. Each anchored region is shrunk by the surface tension pulling along the ventral inner cavity wall conforming to a round- or oval-shaped crystallized spot. The bisected crystallized spots are likely attributed to the secondary crack that occurred at a later time than the primary cracks. The noncircular forming of the central crystallized spot is resulted from non-axisymmetric competition of surface tension pulling associated with the multiple and distributed inner cavity growth.

While Fig. 3.18b shows the non-destructive *SPR* fingerprint of the cavity structure, Fig. 3.18c shows an intrusive image of the crystallized spots after the bulky roof layer has been shattered off. This open view concurs with the non-destructive *SPR* image for the overall locations, shapes, and sizes of the crystallized inner structures, but with noticeably reduced details because of damages and disturbances imposed on the delicate inner structures during the top roof removal. More detrimentally this intrusive examination did not allow imaging of the detailed structure of the peripheral edge region because the top roof could not be separated without destroying the inner structures there.

Figure 3.18d shows non-destructive *R-G-B* fringe imaging (at λ = 635 nm, 535 nm, and 465 nm, respectively) of the hidden cavity structures; these fringes are constructed by interference of the rays reflected from the substrate surface (gold) and rays reflected from the ventral cavity inner surface, and they present quantitative

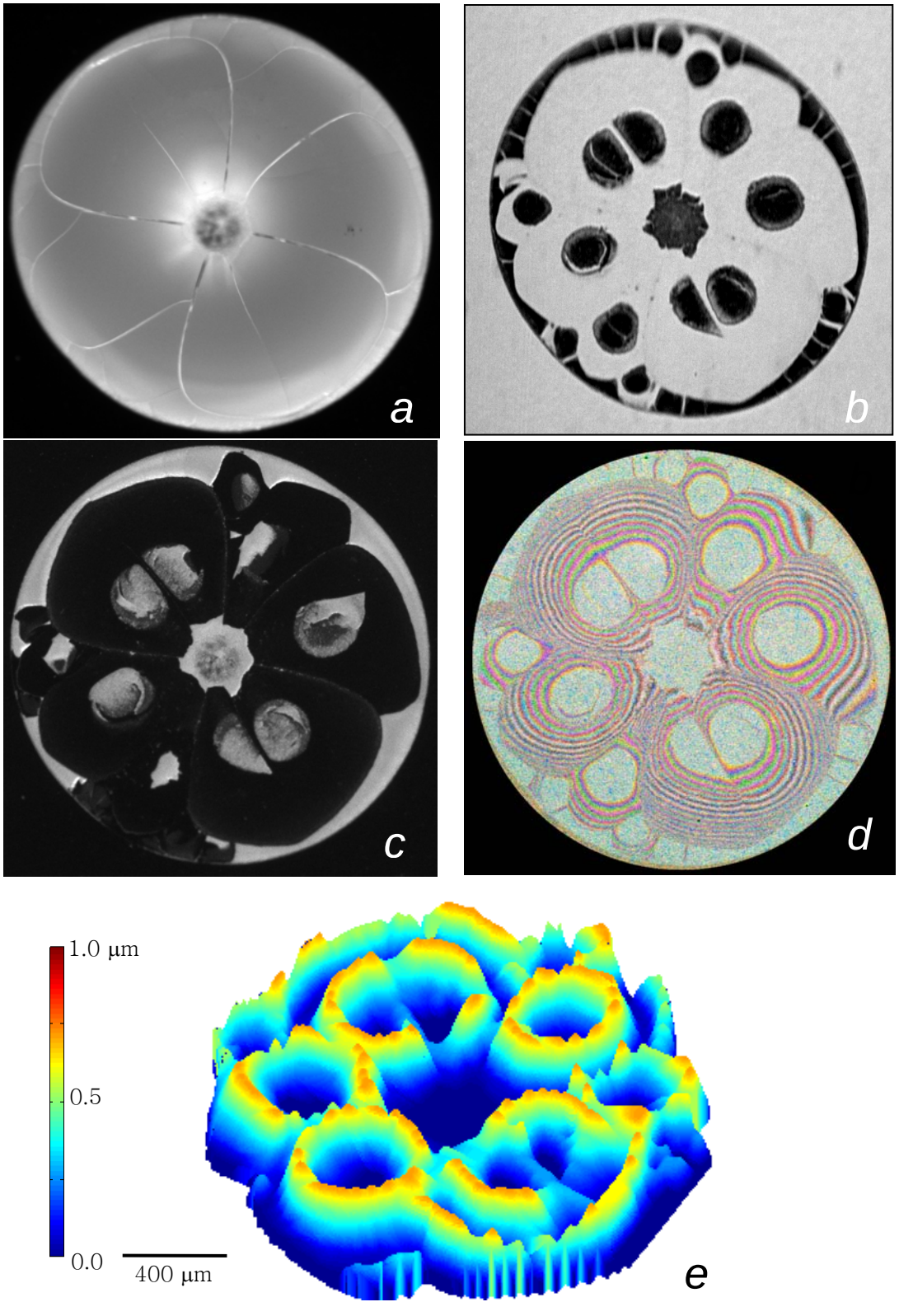
a
b
c
d
1.0 µm
0.5
0.0
400 µm
e

Figure 3.18 Anatomy of a self-assembled nanocrystalline structure revealing the hidden hollow complex cavities formed when a 2-μl aqueous droplet containing 10% volume of 47-nm diameter Al_2O_3 nanoparticles was allowed to evaporate at ambient temperature (21±0.5°C) and humidity (40%) on a gold surface. The microscopic dorsal view **(a)** shows the crystallized half-toroidal glassy surface of approximately 2.0-mm diameter and 160-μm maximum height. Nonintrusive fingerprints by the near-field *SPR* imaging **(b)** clearly evidence the existence of the hidden hollow cavity structures. Note that each cell bounded by crack lines is crystallized to form a single anchoring onto the gold substrate. The destructive image taken with the roof shattered **(c)** confirms the *SPR* fingerprints, but lacks the details particularly in the self-pinned edge region. Naturally occurring *R-G-B* interference fringe map **(d)** is constructed by incident ray interference when they are reflected from both the ventral inner cavity surface and the gold substrate surface, which carry quantitative information on the cavity dimensions. Finally, three-dimensional reconstruction **(e)** of the *R-G-B* fringe map from the computer analysis of (d) unveils the hidden complex cavity structures and completes the detailed 3-D topography showing the maximum vertical scale of 0.72 μm while the maximum crest roof thickness reaches 160 μm [Note that the vertical scale is exaggerated by 400 times compared with the horizontal scale.] [81].

information on the three-dimensional details of the cavity. Two neighboring fringes of an identical color represent the locations where the cavity height differential is equal to $\lambda/4$ [4]. In addition, the spectral sequence of the fringes determines the slope of the inner cavity walls; the slope increases when fringes are seen in the order of …-*B*-*G*-*R*-*B*-*G*-*R*-…, and the slope decreases when fringes are seen as …-*B*-*R*-*G*-*B*-*R*-*G*-…[96]. Therefore, a digital image processing of the fringes shown in Fig. 3.18d allows reconstruction of a full three-dimensional layout of the cavity structure. Furthermore, dynamic recording of the fringe field provides comprehensive knowledge of the time-dependent cavity growth.

Figure 3.18e shows three-dimensional reconstruction of the fringe map of Fig. 3.18d using elaborate pixel-by-pixel analyses and artificially intelligent slope mapping to unveil, for the first time, the hidden complex cavities formed inside the self-assembled nanocrystalline structures. The maximum gap height corresponding to the cavity ridges is approximately 720 nm, which occupies approximately 0.5% of the crystallized crust total height of 160 μm. Note that the vertical scale of the reconstructed topography is exaggerated by 400 times compared with the horizontal scale to present the cavity structure more clearly. It is notable that the topography of the crystallized cavity structures of nanofluids remarkably resembles the earth formation of mountains and valleys.

3.5.3 Summary

We have discovered, using both *SPR* near-field refractive index fingerprinting and natural *R*-*G*-*B* fringe mapping, that hidden hollow cavities exist under nanocrystalline crust structures and the cavities are formed in complex dimensions due to the competing growth of multiple cavities during the evaporative nanocrystalline process. Further, and significantly, the outcome of our research methodology allows us to dynamically examine the self assembly process of the nanocrystalline inner structures and also sheds light on finding a way to actively control the nanocrystalline assembly quality, for example, such as a fabrication of nanofluidic self-assembly with zero-cavity tolerated ensuring the interfacial uniformity. Despite our exhaustive effort associated with careful examination of the fully dynamic *SPR* imaging and *R*-*G*-*B* fringe analysis, we were not able to verify

the existence of the microtornadoes-like flow at present.

CHAPTER 4

Conclusion

A novel tool for a label-free mapping of near-field transport properties of micro/nano-fluidic phenomena is developed using surface plamson resonance (*SPR*) reflectance imaging system. The system successfully demonstrates its feasibility as a innovative tool for full-field and dynamic mapping of microscale concentration profiles, near-wall salinity, transient temperature field, hidden hollow cavities formed during nanocrystallne structure self-assembly, and effective refractive index of nanofluids.

The current developed system has the shortcoming of low spatial resolution from triangular prism. However, this problem will be resolved by applying cylindrical prism or objective. In addition, the current system can be coupled with AFM or confocal microscope to provide comprehensive information of test sample as well as *SPR* data.

We believe that *SPR* reflectance imaging technique will significantly contribute to visualization of micro- and sub-micro scale fluidics and heat transfer phenomena such as a study on the nanocrystalline structure formation depending on the difference of surface hydrophobicity and the label-free and real-time visualization of evaporation-induced fluid flow pattern in binary liquids. Furthermore, this technique can be utilized to characterize single molecules and energy transfer between particles in potential applications of nanomedicine and solar energy harvest.

REFERENCES

1. E. R. G. Eckert and R. J. Goldstein, Measurements in heat transfer, McGraw-Hill, New York (1970).
2. N. Rashidnia, R. Balasubramaniam, Measurement of mass diffusivity of miscible liquids as a function of concentration using a common path shearing interferometer, *Exp Fluids* **36**, 619-626 (2004).
3. H. J. Kim, K. D. Kim, J. S. Allen, Examination of ratiometric laser induced fluorescence thermometry for microscale spatial measurement resolution, *Int. J. Heat Mass Tran* **46**, 3967-3974 (2003).
4. E. Hecht, Optics, 4th ed. Addison and Wesley, New York (2002).
5. M. Born, E. Wolf, Principles of Optics; 7th ed. Cambridge University Press: Cambridge (2003).
6. T. L. Ferrell, T. A. Callcott, R. J. Warmack, Plasmons and Surfaces, *Am Sci* **73**, 344-353 (1985).
7. H. Raether, Surface Plasmons, Springer-Verlag, Berlin (1988).
8. K. F. Giebel, C. Bechinger, S. Herminghaus, M. Riedel, U. Leiderer, U. Weiland, M. Bastmeyer, Imaging of cell/substrate constants of living cells with surface plasmon resonance of microscopy, *Biophys J* **76**, 509-516 (1999)
9. J. R. Lakowicz, Radiative decay engineering 3: Surface plasmon-coupled directional emission, *Anal Biochem* **324**, 153-169 (2004).
10. H. J. Lee, Y. Li, A. W. Wark, R. M. Corn, Enzymatically amplified surface plasmon resonance imaging detection of DNA by Exonuclease III digestion of DNA microarrays, *Anal Chem* **77**, 5096-5100 (2005).
11. H. J. Lee, Y. Yan, G. Marriot, R. M. Corn, Quantitative functional analysis of protein complexes on surfaces, *J Physiol* **563.1**, 61-71 (2005).
12. J. Y. Liu, L. Tiefenauer, S. J. Tian, P. E. Nielsen, W. Knoll, PNA-DNA hybridization study using labeled streptavidin by voltammetry and surface plasmon fluorescence spectroscopy, *Anal Chem* **78**, 470-476 (2006)
13. P. I. Nikitin, A. A. Beloglazov, V. E. Kochergin, M. V. Valeiko, T. I. Ksenevich, Surface plasmon resonance interferometry for biological and chemical sensing, *Sensor Actuat B-Chem* **54**, 43-50 (1999).

14. Z. Salomon, H. A. Macleod, G. Tollin, Surface plasmon resonance spectroscopy as a tool for investigating the biochemical and biophysical properties of membrane protein systems, *Biochimica et Biophysica Acta* **1331**, 117-129 (1997).
15. J. S. Yuk, K. Ha, Proteomic applications of surface plasmon resonance biosensors:anaysis of protein arrays, *Exp and Mol Medicine* **37**, 1-10 (2005).
16. J. S. Shumaker-Parry, R. Aebersold, C. T. Campbell , Parallel, quantitative measurement of protein binding to a 120-element double-stranded DNA array in real time using surface plasmon resonance microscopy, *Anal Chem* **76**, 2071-2082 (2004).
17. T. Zhang, H. Morgan, A. S. G. Curtis, M. Riehle, Measuring particle-substrate distance with surface plasmon resonance microscopy, *J Opt A* **3**, 333-337 (2001).
18. W. Knoll, Interfaces and thin films as seen by bound electromagnetic waves, *Annu Rev Phys Chem* **49**, 569-638 (1998).
19. S. N. Kotsev, C. D. Dushkin, I. K. Ilev, K. Nagayama, Refractive index of transparent nanoparticle films measured by surface plasmon microscopy, *Colloid Polym Sc* **281**, 343-352 (2003).
20 H. Morgan, D. M. Taylor, Surface plasmon resonance microscopy: Reconstructing a three-dimensional image, *Appl Phys Lett* **64**, 1330-1331 (1994).
21. P. Nelson, A. G. Frutos, J. M. Brockman, R. M. Corn, Near-infrared surface plasmon resonance measurements of ultrathin films 1. Angle shift and *SPR* imaging experiments, *Anal Chem* **71**, 3928-3934 (1999).
22. B. Chadwick, M. Gal, An optical temperature sensor using surface plasmons, *Jpn J Appl. Phys* **32**, 2716-2717 (1993).
23. W. W. Lam, L. H. Chu, C. L. Wong, Y. T. Zhang, A surface plasmon resonance system for the measurement of glucose in aqueous solution, *Sensor Actuat B-Chem* **105**, 138-143 (2005).
24. R. P. Podgorsek, H. Franke, Optical determinations of molecule diffusion coefficients in polymer films, *Appl Phys Lett* **73**, 2887-2889 (1998).
25. R. P. Podgorsek, H. Franke, Selective optical detection of aromatic vapors, *Appl Optics* **41**, 601-608 (2002).
26. H-P. Chiang, H-T. Yeh, C-M. Chen, J-C. Wu, S-Y. Su , R. Chang, Y-J. Wu, D. P. Tsai, S.

U. Jen, P. T. Leung, Surface plasmon resonance monitoring of temperature via phase measurement, *Opt Comm* **241**, 409-418 (2004).

27. A. K. Sharma, B. D. Gupta, Theoretical model of fiber optic remote sensor based on surface plasmon resonance for temperature detection, *Opt Fiber Tech* **12**, 87-100 (2006).
28. J. Zeng, D. Liang, Z. Cao, Applications of optical fiber *SPR* sensor for measuring of temperature and concentration of liquids, *Proc SPIE* **5855**, 667-669 (2005).
29. E. Hutter, J. H. Fendler Exploitation of localized surface plamon resonance, *Adv Mater* **16**, 1685-1706 (2004).
30. M. J. Natan, L. A. Lyon, Surface Plasmon Resonance biosensing with colloidal Au amplications. In: Feldheim DL, Foss CA (eds) Metal Nanoparticles, Marcel Dekker, New York: 183-205 (2002).
31. I. I. Smolyaninov, A far field optical microscope with nanometer-scale resolution based on in-plane surface plasmon imaging, *J Opt A* **7**, S165-S175 (2005).
32. I. I. Smolyaninov, C. C. Davis, J. Elliot, A. V. Zayats, Resolution enhancement of a surface immersion microscopy near the plasmon resonance, *Opt Lett* **30**, 382-384 (2005).
33. I. I. Smolyaninov, J. Elliot, A. V. Zayats, C. C. Davis, ar field optical microscope with a nanometer-scale resolution based on the in-plane imaging magnification by surface plasmon polarizations, *Phys Rew Lett* **94**, 057401-1-4 (2005).
34. E. Z. Kretschmann, Die Bestimmung optisher Konstanten von Metallen durch Anregung von Oberfachenplasmaschwingungen, *Physik* **241**, 313-324 (1971).
35. H. Raether, Surface Plasma oscillations and their application. In: Hass G, Francombe MH, Hoffmann RW (eds) Physics of Thin Films, vol **9**: Academic, New York, pp145-261 (1977).
36. H. P. Ho, W. W. Lam, Application of differential phase measurement technique to surface plasmon resonance sensors, *Sensor Actuat B-Chem* **96**, 554-559, (2003).
37. Y. Xinglong, W. Dingxin, W. Xing, D. Xiang, L. Wei, Z. Xinsheng, A surface plasmon resonance imaging interferometry for protein micro-array detection, *Sensor Actuat B-Chem* **108**, 765-771 (2005).
38. J. Zhang, Q. Dai, G. P. Wang, Surface plasmon interferometric microscopy for three-

dimensional imaging of dynamic processes, *Opt Lett* **31**, 3004-3006 (2006).

39. I. Gryczynski, J. Malicka, Z. Gryczynski, K. Nowaczyk , J. R. Lakowicz, Ultraviolet surface plasmon-coupled emission using thin aluminum films, *Anal Chem* **76**, 4076-4081, (2004).
40. T. Libermann, W. Knoll, Surface-plasmon field enhanced fluorescence spectroscopy, *Colloids and Surface* **171** 115-130 (2000).
41. T. Neumann, M-L. Johansson, D. Kambhampati, W. Knoll, Surface-plasmon luorescence spectroscopy, *Adv Funct Mater* **12**, 575-586 (2002).
42. C. E. H. Berger, R. P. H. Kooyman, J. Greve, Resolution in surface plasmon microscopy, *Rev Sci Instrum* **65**, 2829-2836 (1994).
43. J. M. Brockman, B. P. Nelson, R. M. Corn, Surface plasmon resonance imaging measurements of ultrathin organic films, *Annu Rev Phys Chem* **51**, 41-63 (2000).
44. B. Rothenhausler, W. Knoll, Surface Plasmon Microscopy, *Nature* **332**, 615-617 (1988).
45. P. G. Venkata, M. M. Aslan, M. P. Menguc, G. Videen, Surface plasmon scattering patterns of gold nanoparticles and 2D agglomerates, *J Heat Trans* **129**, 60-70 (2007).
46. E. A. Hawes, J. T. Hastings, C. Crofcheck, M. P. Menguc, selective heating of nanosized particles by surface. plasmon resonance, *J Quant. Spectrosc Ra* **104**, 199-207 (2007).
47. E. Fu, T. Chinowsky, J. Foley, J. Weinstein, P. Yager, Characterization of a wavelength-tunable surface plasmon resonance microscope, *Rev Sci Instrum* **75**, 2300-2304 (2004).
48. R. Slavik, J. Homola, Ultrahigh resolution long range surface plasmon-based sensor, *Sensor Actuat B-Chem* **123**, 10-12 (2007).
49. R. H. Richie, Plasma Losses by East Electrons in Thin Films, *Physical Review* **106**, 874-881 (1957).
50. A. E. Kryukov, Y-K. Kim, J. B. Kettersonb, Surface plasmon scanning near-field optical Microscopy, *J Appl Phys* **82**, 5411-5415 (1997).
51. K. Kurihara, K. Suzuki, Theoretical understanding of an absorption-based surface plasmon resonance sensor based on Kretchmann's theory, *Anal Chem* **74**, 696-701 (2002).

52. H.-P. Chiang, P. T. Leung, W. S. Tse, The surface Plasmon enhancement effect on absorbed molecules at elevated temperatures, *J Chem Phys* **108**, 2659-2660 (1998).
53. S. K. Ozdemir, G. T.-S., Temperature effects on surface lasmon resonance: Design considerations for an optical temperature sensor, *J. Lightwave Technol* **21**, 805-814 (2003).
54. A. A. Kolomenskii, P. D. Gershon, H. A. Schuessler, Sensitivity and detection limit of concentration and adsorption measurements by laser-induced surface-plasmon resonance, *Applied Optics* **36**, 6539-6547 (1997).
55. T. Inagaki, K. Kagami, C. T. Arakawa Photoacoustic observation of nonradiative decay of surface plasmons in silver, *Phys Rev B* **24**, 3644-3646 (1981).
56. Rothenhausler, J. Rabe, P. Korpiun, W. Knoll, On the decay of plasmon surface polaritons at smooth and rough Ag-air interfaces: A reflectance and photo-acoustic study, *Surface Sci* **137**, 373-383 (1984).
57. D-L. Hornauer, Light scattering experiments on silver films of different roughness using surface plasmon excitation, *Opt Commun* **16,** 76-79 (1976).
58. I. T. Kim, K. D. Kihm, Label-free visualization of microfluidic mixture concentration fields using a surface Plasmon resonance (*SPR*) reflectance technique, *Exp. Fluids* **41**, 905-916 (2006).
59. I. T. Kim, K. D. Kihm, Surface plasmon resonance (*SPR*) reflectance imaging: A label-free/real-time mapping of microscale mixture concentration fields (Water+Ethanol), *Journal of Heat Transfer* **129**, 930 (2007).
60. I. T. Kim, K. D. Kihm, Label-free detection of full-field microfluidc concentration and temperature Fields by surface plasmon resonance (*SPR*) reflectance imaging technique, 18th International Symposium on Transport Phenomena (ISTP-18), Daejon, Korea, Aug. 27-30, pp.244-258 (2007).
61. D. R. Lide, CRC Handbook of Chemistry and Physics; CRC Press; 85th ed., Electronic Edition (2005).
62. E. Moreels, C. de Greef, R. Finsy, Laser light refractometer, *Appl Optics* **23**, 3010-3013 (1984).
63. R. Belda, J. V. Herraez, O. Diez, A study of the refractive index and surface tension

synergy of the bianry water/ethanol:influence of concentration, *Phys Chem Liq* **43**: 91-101 (2005).

64. J. S. Allen, K. P. Hallinan, J. Lekan, A study of the fundamental operations of a capillary driven heat transfer device in both normal and low gravity: part 1 Liquid slug formation In low gravity, *AIP Conference Proceedings* **420**, 471-478 (1998).
65. K. D. Kihm, A. Banerjee, C. K. Choi, T. Takagi, Near-wall hindered Brownian diffusion of nanoparticles examined by three-dimensional ratiometric total internal reflection fluorescence microscopy (3-D R-*TIRFM*), *Exp Fluids* **37**, 811-824 (2004).
66. S. J. Kline, F. A. McClintock, Describing uncertainties in single-sample experiments, *Mechanical Engineering* **75**, 3-8 (1953).
67. P. B. Johnson, R. W. Christy, Optical Constants of the Noble Metals, *Phys Rev B* **6**, 4370-4379 (1972).
68. Jones, S.; Bautz, M.; Kissel S.; Pivovaroff, M. Using tritium and X-ray tubes as X-ray calibration sources for the AXAF CCD imaging spectrometer, *Proc. SPIE*, ***2808***, 158-169 (1996).
69. I. T. Kim, K. D. Kihm, Real-time and full-field detection of near wall Salinity using surface Plasmon (*SPR*) reflectance, *Anal. Chem* **79**, 5418-5423 (2007).
70. I. Kim, K. D. Kihm, Label-Free and Near-Field Mapping of Molecular diffusion (Saline Solution/Water) Using Surface Plasmon Resonance (*SPR*) Refractive Index Field Imaging, *Journal of Heat Transfer* **130**, 080906-1 (2008).
71. I. T. Kim, K. D. Kihm, Label-free imaging of temperature fields using surface plasmon resonance (*SPR*) reflectance, *Opt. Letters*, **32**, 3456-3458 (2007).
72. J. J. Thomson, H. F. Newall, On the Formation of Vortex Rings by Drops falling into Liquids, and some allied Phenomena, *Proc. Royal Soc*. **39**, 417-436 (1885).
73. D. D. Joseph, Fluid dynamics of two miscible liquids with diffusion and gradient stresses, *Eur. J. Mech., B/Fluids* **9**, 565-596 (1990).
74. E. D. Palik, Handbook of Optical Constants of Solids, Academic Press (1985).
75. K. A. Peterlinz, R. Georgiandis, In situ kinetics of self-assembly by surface plasmon resonance spectroscopy, *Langmuir* **12,** 4731 (1996).
76. B. A. Snopok, K. V. Kostyukevich, S. I. Lysenko, P. M. Lytvyn, O. S. Lytvyn, S.V.

Mamykin, S. A. Zynyo, P. E. Shepeliavyi, S. A. Kostyukevich, Yu. M. Shirshov, and E. F. Venger, Optical biosensors based on the surface Plasmon resonance phenomenon, Semiconductor Physics, Quantum Electronics & Optoelectronics **4**, 56 (2001).

77. K. Alexander, A. Killey, G. Meeten, M. Senior, *J Chem Soc Faraday Trans,* Refractive index of concentrated colloidal dispersions **77**, 361-372 (1981).
78. C. H. Chon, K. D. Kihm, S. P. Lee, S. U. S. Choi, Empirical correlation finding the role of temperature and particle size for nanofluid (Al2O3) thermal conductivity enhancement, *Appl Phys Lett* **87**, 153107 (2005).
79. K.-E. Peiponen, A. Jaaskelainen, J. Raty, O. Richard, U. Tapper, E. I. Kauppinen, K. Lumme, Reflectance study of pigment slurries, *Appl Spectrosc* **54**, 878 (2000).
80. M. Mohammadi, Colloidal refraactometry, *Adv Colloid Interface Sci* **62**, 17 (1995).
81. I. Kim, K. D. Kihm, Full-field and real-time surface Plasmon resonance imaging thermometry, *Langmuir* (On-line published as of Aug. 29, 2008).
82. G. H. Meeten, A. N. North, Refractive index measurement of absorbing and turbid fluids by reflection near the critical angle, *Meas Sci Technol* **6**, 214 (1995).
83. Y. E. Sarov, I. Capek, T. B. Ivanov, K. Z. Ivanov, V. A. Sarov, I. W. Rangelow, On total internal reflection investigation of nanoparticles by integrated micro-fluidic system, *Nano Lett* **8**, 375 (2008).
84. I. Kim, K. D. Kihm, Surface Plasmon resonance reflectance correlation with near-field effective RI of nanofluids (47 nm Al2O3 nanofluids) (under preparation for *Applied Physics Letters or Nano Letters*).
85. V. Champion, G. H. Meeten, M. Senior, Refraction by spherical colloid particles, *J Colloid Interf Sci* **72**, 471 (1979).
86. R. H. French, H. Mullejans, D. J. Jones, Optical properties of alumina oxide, *J Am Ceram Soc* **81**, 2549 (1998).
87. H. C. van de Hulst, Light Scattering by Small Particles, Dover (1957).
88. R. D. Deegan, O. Bakajin, T. F. Dupont, G. Huber, S. R. Nagel, T. A. Witten, Capillary-Flow as the Cause of Ring Stains from Dried Liquid-Drops, *Nature***, 389**, 827 (1997**).**

89. G. M. Whitesides, B. Grzybowski, Self-assembly at all scales, *Science* **295***,* 2418-2421 (2002).
90. T. P. Bigioni, X.-M. Lin, T. T. Nguyen, E. I. Corwin, T. A. Witten, H. M. Jaeger, Kinetically driven self assembly of highly ordered nanoparticle monolayers, *Nature Materials* **5**, 265-270 (2006).
91. E. Rabani, D. R. Reichman, P. L. Geissler, L. E. Brus, Drying-mediated self-assembly of nanoparticles, *Nature* **426**, 271-274 (2003**).**
92. J. Xu, J. Xia, Z. Lin, Evaporation-Induced Self-Assembly of Nanoparticles from a Sphere-on-Flat Geometry, *Angew Chem* **119**, 1892-1895 (2007).
93. S. W. Hong, J. Xu, Z. Lin, Template assisted formation of gradient concentric gold rings, *Nano Lett* **6**, 2949-2954 (2006).
94. A. P. Sommer, Microtornadoes under a nanocrystalline Igloo, *Cryst Growth Des* **7,** 1031-1034 (2007).
95. A. P. Sommer, D. Zhu, Microtornadoes under a nanocrystalline Igloo, *Cryst. Growth Des* **7**, 2373-2375 (2007).
96. K. D. Kihm, D. M. Pratt, Thickness and slope measurements of evaporative thin liquid film, *J Heat Trans* **121,** Heat Transfer Gallery (1999).
97. C. H. Chun, S. W. Paik, J. Tipton, K. D. Kihm, Effect of Nanoparticle Sizes and Number Densities on the Evaporation and Dryout Characteristics for Strongly Pinned Nanofluid Droplets, *Langmuir* **23**, 2953-2960 (2007).
98. L. Motte, E. Lacaze, M. Maillard, M. P. Pileni, Self-assembly of silver sulfide nanocrystals on various substrates, *Langmuir* **16**, 3803-3812 (2000).
99. Z.-Z. Gu, Y.-Hu. Yu, H. Zhang, H. Chen, Z. Lu, A. Fujishima, O. Sato, Self-assembly of monodisperse spheres on substrates with different wettability, *Appl.Phys. A* **81**, 47-49 (2005).
100. A. P. Sommer, N. Rozzlosnik, Formation of crystalline ring patterns on extremely hydrophobic supersmooth substrates, *Cryst Growth Des* **5**, 551-557 (2005).
101. R. D. Deegan, O. Bakajin, T. F. Dupont, G. Huber, S. R. Nagel, T. A. Witten, Contact line deposits in an evaporating drop, *Phys. Rev. E* **62**, 756-765 (2000).
102. H. Hu, R. G. Larson, Marangoni Effect Reverses Coffee-Ring Depositions, *J Phys*

Chem B **110**, 7090-7094 (2006).

103. X. Xu, J. Luo, *Appl Phys Lett* **91**, 124102 (2007).

104. Israelachvili, J. N. *Intermolecular and Surface Forces;* Academic Press: San Diego, (1992).

105. A. G. Nnanna, Experimental model of temperature-driven nanofluid, *J Heat Trans-T. ASME* **129**, 697-704 (2007).

106. M. Maillard, L. Motte, A. T. Ngo, M. P. Pileni, Rings and hexagons of nanocrystals, *J. Phys. Chem. B.* **104**, 11871-11877 (2000).

107. R. Duggal, F. Hussain, M. Pasquali, Self-assembly of single-walled carbon nanotubes into a sheet by drop drying, *Adv Mater* **18**, 29-34 (2006).

108. L. Pauchard, C. Allain, Mechanical instability induced by complex liquid desiccation, *C R Physique* **4**, 231-239 (2003).

109. J. Wang, R. G. Evans, Drying behaviour of droplets of mixed powder suspensions, *J. Eur. Ceram. Soc.* **26**, 3123-3131 (2006).

110. M. D. Haw, M. Gillie, W. C. Poon, Effects of phase behavior on the drying of colloidal suspensions, *Langmuir* **18**, 1626-1633 (2002).

APPENDIX

Fresnel Calculation Program (Matlab)

```
% Calculate the Fresnel equation and penetration depth, lateral resolution
% written by Iltai Kim in MINSFET laboratory, University of Tennessee
% Sept. 7, 2008

clear all;
% write data file with theta loop
%fid_theta=fopen('SF10.dat','w');
% write data file with n_m loop
fid_n_m=fopen('SF10_n_m.dat','w');

% refractive index n; 2 is prism, 1 is adhesion layer, 3 is thin metal film
n(2)=1.7231; % SF10 prism
%n(2)=1.515; % BK7 prism
n(3)=0.1718+i*3.637; % Au
n(1)=n(3);       % for (1) test medium

% wavelength of incoming light
lumda=632.8*10^-9; % in meter

% Thickness of adhesion layer (1) and thin metal film(3) in meter
d1=2.5*10^-9;
d3=45.0*10^-9;

% refractive index of water with temperature 0~100 degree
n_m_org=[1.33306 1.33211 1.32972       1.32636 1.32223 1.31744];

theta(1)=56.3; % incident angle for initial calculation

i_n=1; % for example, one data is used in the following program
n_m(i_n)=n_m_org(i_n);

% Loop with refractive index of test medium
for i_n_m=1:1:200
      n_t(i_n_m)=0.01*i_n_m;
      n_m(i_n)=n_t(i_n_m);
      % Loop with theta increment
      %for i_theta=1:1:700
      %       theta(i_theta)=theta(1)+0.1*i_theta;
      i_theta=1;

      n(4)=n_m(i_n); % test medium

      for j= 1:4
```

```
        e(j)=n(j)^2;
    end

    e(5)=e(4)*e(1)/e(3);

    k_sp=2*pi/lumda*sqrt( (e(3)*e(4))/(e(3)+e(4))); % wavevector of SP
    k_x=(2*pi/lumda)*sqrt(e(2))*sin(theta(i_theta)*pi/180.); % wavevector of x-
component

    for j=1:4
        const1=e(j).*(2*pi/lumda)^2;
        const2= k_x.*k_x;
        const3=const1-const2;
        k(j)=sqrt(e(j).*(2*pi/lumda)^2 - k_x.*k_x);
    end

    k(5)=k(4)*k(1)/k(3);

    n53=e(3)*k(5)+e(5)*k(3);
    n21=e(1)*k(2)+e(2)*k(1);
    n14=e(4)*k(1)+e(1)*k(4);

    z53=e(3)*k(5)-e(5)*k(3);
    z14=e(4)*k(1)-e(1)*k(4);
    z21=e(1)*k(2)-e(2)*k(1);

    r134=(z14-i*z53*tan(k(3)*d3))/(n14-i*n53*tan(k(3)*d3));
    r21=z21/n21;
    r214=(r21+r134*exp(2*i*k(1)*d1))/(1+r21*r134*exp(2*i*k(1)*d1));

    R(i_n_m)=abs(r214)^2; % Reflectance
    fprintf(fid_n_m,' %6.4f %6.4f ',n_t(i_n_m), R(i_n_m));
    fprintf(fid_n_m,'\n');

    L(i_n)=1/(2*imag(k_sp))*10^6;    % propagation length of SP wave
    %i_n=i_n+1;
end
figure(1)
plot(n_t, R)

fclose(fid_n_m);
```

VITA

Iltai Kim was born in Seoul, South Korea on Sptember 6, 1969. After graduating from Kongju National Teachers' Associate High School in 1988, he entered Pohang University of Science and Technology (POSTECH) in Pohang, South Korea and received a B.S. degree in 1992 and a M.S. degree in Mechanical Engineering at POSTECH in 1994, respectively. His undergraduate advisor was the late Dr. C.M. Lee, and Dr. Chung-Hwan Chun and Dr. K. Y. Huh supervised his master degree work. After graduation, he joined Pohang Iron and Steel Company (POSCO), one of the largest and the most competitive iron & steel manufacturers in the world, and worked as a research engineer for ten years in the field of thermal/fluidic engineering.

His doctorate study in Mechanical Engineering began at Texas A & M University in College Station, TX in August 2003, and he transferred to the University of Tennessee, Knoxville in August 2004 with his advisor Dr. Kihm. Successfully completing all requirements toward his doctoral degree at the Micro/Nano-Scale Fluidics and Energy Transport Laboratory, he received his doctoral degree in December 2008 at the University of Tennessee, Knoxville under the supervision of his advisor, Dr. Kenneth D. Kihm, Magnavox Chair Professor in Mechanical, Aerospace and Biomedical Engineering Department.